


# Colloquium: Sliding and pinning in structurally lubric 2D material interfaces

Jin Wang 

*International School for Advanced Studies (SISSA), Via Bonomea 265, 34136 Trieste, Italy*

Ali Khosravi 


*International School for Advanced Studies (SISSA), Via Bonomea 265, 34136 Trieste, Italy  
and International Centre for Theoretical Physics (ICTP),  
Strada Costiera 11, 34151 Trieste, Italy*

Andrea Vanossi 

*CNR-IOM, Consiglio Nazionale delle Ricerche—Istituto Officina dei Materiali,  
c/o SISSA, Via Bonomea 265, 34136 Trieste, Italy  
and International School for Advanced Studies (SISSA),  
Via Bonomea 265, 34136 Trieste, Italy*

Erio Tosatti \*

*International School for Advanced Studies (SISSA), Via Bonomea 265, 34136 Trieste, Italy,  
International Centre for Theoretical Physics (ICTP), Strada Costiera 11, 34151 Trieste, Italy,  
and CNR-IOM, Consiglio Nazionale delle Ricerche—Istituto Officina dei Materiali,  
c/o SISSA, Via Bonomea 265, 34136 Trieste, Italy*

 (published 7 February 2024)

A plethora of two-dimensional (2D) materials have been introduced in physics and engineering in the past two decades. Their robust, membranelike sheets permit (mostly require) deposition, giving rise to solid-solid dry interfaces whose mobility, pinning, and general tribological properties under shear stress are currently being understood and controlled, both experimentally and theoretically. In this Colloquium simulated case studies of twisted graphene systems are used as a prototype workhorse tool to demonstrate and discuss the general picture of 2D material interface sliding. First highlighted is the crucial mechanical difference, often overlooked, between small and large incommensurabilities, which corresponds to, for example, small and large twist angles in graphene interfaces. In both cases, focusing on flat, structurally lubric or “superlubric” geometries, the generally separate scalings with the area of static friction in pinned states and of kinetic friction during sliding are elucidated and reviewed, tangled as they are with the effects of velocity, temperature, load, and defects. The roles of island boundaries and elasticity are also discussed, and compared when possible to results in the literature for systems other than graphene. It is proposed that the resulting picture of pinning and sliding should be applicable to interfaces in generic 2D materials that are of importance for the physics and technology of existing and future bilayer and multilayer systems.

DOI: [10.1103/RevModPhys.96.011002](https://doi.org/10.1103/RevModPhys.96.011002)

## CONTENTS

I. Introduction	2	V. Area Dependence	10
II. Static Structure of 2D Twisted Interfaces	4	VI. Velocity and Temperature	12
A. Three regimes	4	VII. Load	14
B. Understanding the relaxed structural regimes	4	A. Ordinary and differential friction coefficients	14
III. Twisted Graphene Interface Simulations:		B. Friction coefficient of 2D material interfaces	16
A demonstration tool	5	VIII. Elasticity	17
IV. Simulated 2D Sliding Friction	7	IX. Defects	19
A. Static friction and energy barriers	7	A. Shape of sliders	19
B. Kinetic friction: Surfing moiré	8	B. Grain boundaries	20
		C. Step edges	20
		D. Contaminants	20
		X. Summary	20
		Acknowledgments	22
		References	22

\*tosatti@sissa.it

## I. INTRODUCTION

A great variety of stiff, graphenelike 2D materials, qualitatively displayed in Figs. 1(a)–1(c) (Geim and Novoselov, 2007; Geim and Grigorieva, 2013; Novoselov *et al.*, 2016), increasingly pervades materials science, physics, and technology. This includes graphene bilayers and transition metal dichalcogenides that are especially important for new phenomena and applications (Rao *et al.*, 2009; Butler *et al.*, 2013; Geim and Grigorieva, 2013; Liu *et al.*, 2016; Novoselov *et al.*, 2016; Wang, Ma, and Sun, 2017; Yankowitz, Ma *et al.*, 2019; Pham *et al.*, 2022).

Besides the electronic properties that attract most of the attention (Cao *et al.*, 2018; Cao, Fatemi *et al.*, 2018; Kerelsky *et al.*, 2019; Yankowitz, Chen *et al.*, 2019; Stepanov *et al.*, 2020; Park *et al.*, 2021), their mechanical, tribological, and rheological characterization must in parallel be physically understood and controlled (Zhang *et al.*, 2019), for many reasons. A first, practical one is that mutual sliding of two juxtaposed 2D material layers is known to be easy owing to their weak interlayer van der Waals interaction. Beyond that, mutual incommensurability of 2D material interfaces can lead to ultralow sliding friction, a property known as “superlubricity” (Hirano and Shinjo, 1990; Dienwiebel *et al.*, 2004). That property makes it naturally attractive for energy saving, and potentially for lifetime increase. Manipulations involving these interfaces also occur in several microscale and nanoscale experiments; see Fig. 1(d). Good lubricity makes them promising for the application in microelectromechanical and nanoelectromechanical systems such as microgenerators, nanogenerators, and nano-oscillators (Zheng and Jiang, 2002; Huang, Lin, and Zheng, 2020; Huang *et al.*, 2021; Wu *et al.*, 2021). Another, more substantial reason is that our current understanding of superlubricity is still too vague. On the whole, the friction’s connection to incommensurability and rotation is, as we later see, a source of surprises.

The general incommensurate interface of 2D materials is composed of two monolayers that either are identical but rotated by a “twist” angle  $\theta$  (homostructure case) or are different, with an inherent lattice mismatch (heterostructure case). It is characterized by the so-called moiré pattern [see Figs. 2(a)–2(c)], an almost-periodic superlattice resulting from

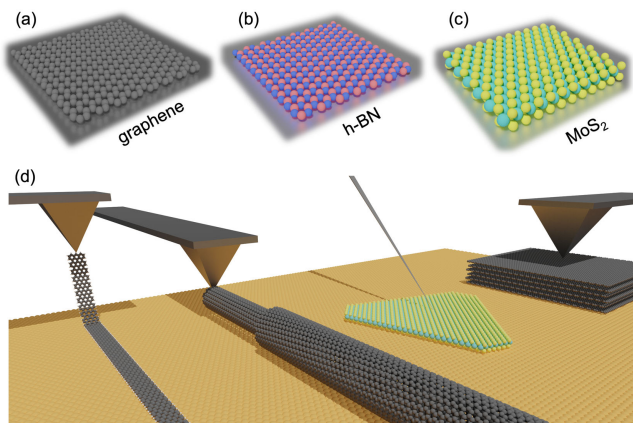


FIG. 1. (a)–(c) Some relevant 2D materials. (d) Common experimental setups involving their interfaces.

the beating of the two 2D lattices. The lattice constant of the moiré superlattice  $\lambda$  between layers with triangular or hexagonal symmetry is determined by the lattice constants of the two contacting layers  $a$  and  $b$  and the twist angle  $\theta$ ,

$$\lambda(\theta) = \frac{ab}{\sqrt{a^2 + b^2 - 2ab \cos(\theta)}}. \quad (1)$$

For homostructures with  $a = b$ , the moiré size  $\lambda(\theta) = a/\sqrt{2 - 2\cos\theta}$  scales as  $\theta^{-1}$ . When one of the layers (the “slider”) is sheared relative to the other, the moiré pattern drifts at an angle  $\beta$  relative to the sliding direction,

$$\beta(\theta) = \arccos \frac{b - a \cos(\theta)}{\sqrt{a^2 + b^2 - 2ab \cos(\theta)}}. \quad (2)$$

As Eq. (2) shows, the moiré pattern generally drifts askew of the sliding direction. The ratio of the sliding velocity of the moiré  $v_M$  to the slider’s  $v$  is  $\lambda/a$  (Hermann, 2012; Wang, Ma, and Tosatti, 2023). Larger than 1, this ratio diverges when  $a = b$  and  $\theta \rightarrow 0^\circ$ . As sketched in Figs. 2(d)–2(f), for graphene/graphene homostructures, and thus with  $a = b$  and twist angle  $\theta$ ,  $\beta = 90^\circ - \theta/2$ , i.e., the moiré direction is nearly perpendicular to the sliding direction of the slider at small twists. For a heterostructure bilayer such as *h*-BN/graphene with mismatched lattices  $a/b \approx 1.018$  at zero twist angle [Figs. 2(g)–2(i)],  $\beta = 180^\circ$ .

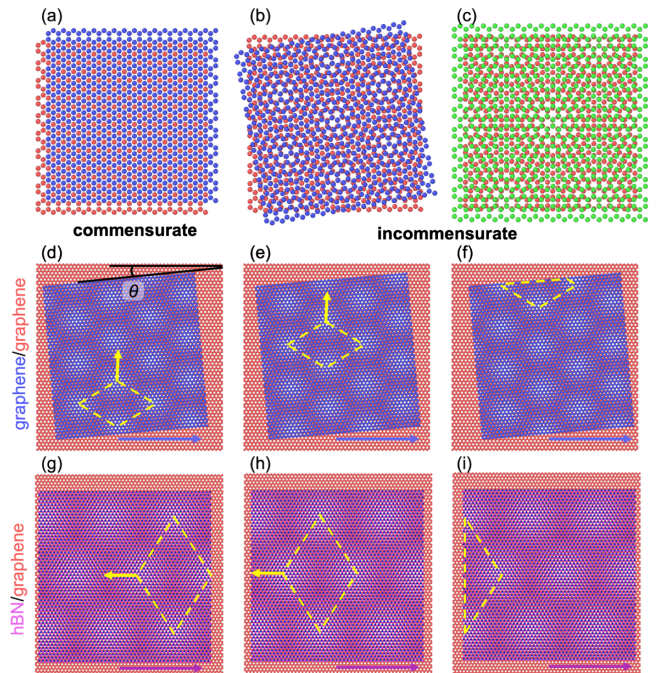


FIG. 2. Sketch of 2D material interfaces. (a) Commensurate and (b) “homo” incommensurate with twist angle  $\theta$ . (c) “Hetero” incommensurate with lattice mismatch  $a \neq b$  and zero twist. (d)–(f) Graphene-graphene moiré cell (dashed-line rhombi), shown for a small twist  $\theta$ , obliquely translating upon horizontal interface sliding (arrow). (g)–(i) Same approach for *h*-BN/graphene when  $\theta = 0$ . The angle of motion of the moiré lattice relative to the graphene lattice is  $\beta$  [Eq. (2)].

A host of questions arise about the facile sliding of these incommensurate 2D crystalline interfaces, or alternatively about their mechanical pinning against shear. The exceptional in-plane robustness coupled with great out-of-plane membranelike flexibility are new elements. Another one is the unusually important adhesion between the flat layers. These elements make 2D material interfaces different than other frictional systems (Vanossi, Bechinger, and Urbakh, 2020) such as 3D solids (Liu, Erdemir, and Meletis, 1996; Bowden and Tabor, 2001; Eriksson, Bergman, and Jacobson, 2002; Zhao *et al.*, 2021), adsorbed layers and clusters (He, Müser, and Robbins, 1999; Krim, 2012; Pierno *et al.*, 2015; Varini *et al.*, 2015), and colloid monolayers (Bohlein, Mikhael, and Bechinger, 2012; Vanossi and Tosatti, 2012; Mandelli *et al.*, 2015; Brazda *et al.*, 2018; Cao *et al.*, 2019). In the nanoscale to mesoscale range, the size and temperature dependence of static friction of 2D material contacts, as well as their comparison to that of velocity-dependent kinetic friction generally differs from classic macroscopic laws in a way that is currently addressed case by case. The widespread concept in the sliding of crystalline interfaces is structural lubricity between incommensurate faces (Sokoloff, Sacco, and Weisz, 1978; Aubry, 1983; Peyrard and Aubry, 1983; Müser, 2004), which is generally believed to imply superlubricity (Sokoloff, 1990; Shinjo and Hirano, 1993; Dienwiebel *et al.*, 2004; Vanossi *et al.*, 2013; Baykara, Vazirisereshk, and Martini, 2018; Martin and Erdemir, 2018). Note that this term currently holds different meanings in physics and engineering.

Standard superlubricity (Peyrard and Aubry, 1983), which we adopt here as being synonymous with *structural superlubricity* (Müser, 2004), can be defined for infinite defect-free systems as an *unpinned*, free sliding state; that is, a state where the static friction  $F_s$  (the smallest force needed to initiate the sliding motion) is mathematically zero even down to  $T = 0$ . This also implies the ability to slide, albeit with infinitesimal velocity, under an infinitesimal applied force. In the real world everything has a finite size, even without defects. The edges destroy the slider's perfect translational invariance, inevitably causing static friction. However, if the slider's bulk is structurally superlubric and defect free,  $F_s$  scales as  $A^\alpha$  with  $\alpha \leq 1$ . For  $\alpha < 1$  we refer to this real-world cousin of structural superlubricity here as structural lubricity. Finally, engineers and practitioners who handle real materials with systematic defects, finite temperature, etc., sometimes refer to superlubricity for any system with low sliding friction and friction coefficient ( $\mu < 10^{-2}$ ) (Martin *et al.*, 1993; Baykara, Vazirisereshk, and Martini, 2018; Hod *et al.*, 2018; Martin and Erdemir, 2018). To avoid confusion, which this superposition of names sometimes generates, we use the term *engineering superlubricity* when needed for the latter. Despite the early detection of superlubricity (Hirano *et al.*, 1997; Liu, Yang *et al.*, 2012) in structurally lubric twisted graphene flakes and graphite interfaces (Liu, Erdemir, and Meletis, 1996; Dienwiebel *et al.*, 2004; Filleter *et al.*, 2009; Lee *et al.*, 2010; Liu, Yang *et al.*, 2012; Urbakh, 2013; Berman *et al.*, 2015; Koren *et al.*, 2015; Kawai *et al.*, 2016; Qu *et al.*, 2020) and theoretical work (Consoli, Knops, and Fasolino, 2000; de Wijn, 2012; van den Ende, Wijn, and Fasolino, 2012; Hod, 2013; Leven *et al.*, 2013; Mandelli *et al.*, 2019), the

community remains in need of a broad road map applicable to the sliding of 2D layered materials. We now pose some of the questions that seem currently open and/or debatable.

To what extent does a large twisted bilayer, incommensurate and therefore a candidate for structural superlubricity, or at least to structural lubricity, realize free sliding? What is the origin of friction and how are static and kinetic friction related at 2D material interfaces? What kind of area, temperature, velocity, and load dependence of interface sliding friction should one generally anticipate? Specifically, different experiments report different scaling of friction with area  $A^\alpha$ , with the exponent  $\alpha$  ranging from 0 to 1. What is the origin of this dispersion? What role does the extreme 3D anisotropy of these poorly extensible, yet flexible and easily corrugated membranes play? Why is it that structurally lubric 2D material experimental sliders generally exhibit a logarithmic velocity dependence (the earmark of stick-slip) (Gnecco *et al.*, 2000; Riedo *et al.*, 2003; Müser, 2011) instead of a linear one (the earmark of smooth sliding)? Can temperature (or load) bring about a change between high and low friction states (Krylov and Frenken, 2014; Pellegrini *et al.*, 2019)? And numerically what are the actual friction coefficients of the 2D material interfaces? Are the differential friction coefficients generally used for 2D materials really adequate?

This Colloquium was inspired by questions like these. Answers are currently scarce, despite extensive investigations of a variety of 2D materials and models. We proceed through an examination of successive physical properties, with references to existing literature abundantly augmented by our own simulations. Ultimately we aim to provide a more comprehensive framework for nanofriction of structurally lubric 2D material interfaces. The workhorse helping us throughout our discussion mostly is a graphene/graphene twisted interface. Convenient as it is for a direct exemplification through molecular dynamics simulations, that choice also describes encapsulated bilayers, systems of current interest for their own sake (Andrei and MacDonald, 2020; Mogera and Kulkarni, 2020; Nimbalkar and Kim, 2020; Pham *et al.*, 2022; Törmä, Peotta, and Bernevig, 2022). Beyond the specific example, the scope of our approach is broader. Results should be applicable for generic twisted, structurally lubric, incommensurate contacts among 2D materials (Geim and Grigorieva, 2013; Novoselov *et al.*, 2016), which we consider our broader target.

The Colloquium proceeds as follows. Prior to actual sliding, we first examine in Sec. II the equilibrium interface geometry. That will highlight the existence of qualitatively different configurations as a function of decreasing twist angle: large, intermediate, and small. We then introduce in Sec. III the setup of nonequilibrium molecular dynamics (NEMD) simulations of a twisted graphene interface, modeling the structure and sliding with a state-of-the-art force field. Simulations that, as mentioned, are a tool to embody our questions and to propose answers along with discussion and review. Energy barriers and related static friction considerations, together with simulated frictional force traces, that represent the background data for subsequent analysis are presented in Sec. IV. Section V is devoted to the generally distinct (yet sometimes coincident) area dependencies of static and kinetic friction in different regimes and geometries. Temperature dependence, where viscous friction is characteristic of truly superlubric free

sliding, is contrasted in Sec. VI with the so-called thermolubric evolution, where thermal barrier crossing gradually smears out stick-slip friction. A similar contrast between free sliding and stick-slip regimes shows up in the velocity dependence of kinetic friction, which correspondingly varies from linear to logarithmic. The load dependence of 2D material friction of Sec. VII highlights the concept and nature of the friction coefficient, for which we provide a tentative table. Friction coefficient data of 2D materials are rare in the literature, where only differential friction coefficients usually appear. That point is corrected by considering adhesion, which is unusually important in 2D material contacts. We also clarify that the load dependence of friction in structurally lubric 2D interfaces arises insofar as pressure modifies the barriers created by edges and defects. The effect of interfacial elasticity on static and kinetic friction, which is directly related to the size of the system and particularly important at the mesoscale, is discussed in Sec. VIII. The variety of defects that mix up and modify the frictional properties of clean perfect interfaces is the subject of Sec. IX, where we limit ourselves to the main defects. A discussion and outlook conclude the Colloquium in Sec. X. In the spirit of Colloquia (a Reviews of Modern Physics format invented by Ugo Fano, who was a mentor to one of us), we debate the questions lined up at the outset and do not attempt to offer a scholarly review of the countless contributions to the field.

## II. STATIC STRUCTURE OF 2D TWISTED INTERFACES

### A. Three regimes

Prior to directly addressing tribology, with its resulting shear stress, pinning, and sliding, it is necessary to understand the static structure of a generically incommensurate 2D material crystalline interface, where the moiré patterns do not match the crystal lattices. To begin, the two layers are not rigid and deform statically in order to adapt to each other, bringing the total energy to a minimum. This deformation, which we later detail, is important in all of our discussions. Its nature is a mere structural relaxation, rather than a “reconstruction,” as it is sometimes called (Yoo *et al.*, 2019). In fact, it changes neither the moiré periodicity nor any other symmetry. The deformation consists mostly of out-of-plane  $z$  corrugations of the two layers, stiff in plane but easy to bend. It is unsymmetrical in a heterostructure interface and antisymmetrical across the bilayer’s neutral plane in a homostructure interface at rest.

We employ here the twisted bilayer graphene (TBG), simulated as detailed in Sec. III, as the simplest showcase of the relaxed structure; see Fig. 3. Generally there are different regimes to the structure of a 2D material interface. In a TBG they are realized as a function of the twist angle  $\theta$ : large ( $L$ ), intermediate ( $I$ ), and small ( $S$ ), as described in Figs. 3(a) and 3(b). In the first regime  $L$ , with the twist  $\theta$  ranging from  $30^\circ$  down to about  $10^\circ$ , the moiré pattern with small lateral size  $\lambda(\theta)$  is accompanied by an out-of-plane corrugation  $z(x, y)$ . Here  $z$  is sinusoidal in shape and of a small magnitude relative to the interlayer spacing, while it grows moderately for decreasing  $\theta$ . In the opposite small twist regime  $S$  below  $3^\circ$ , the corrugation pattern differs completely

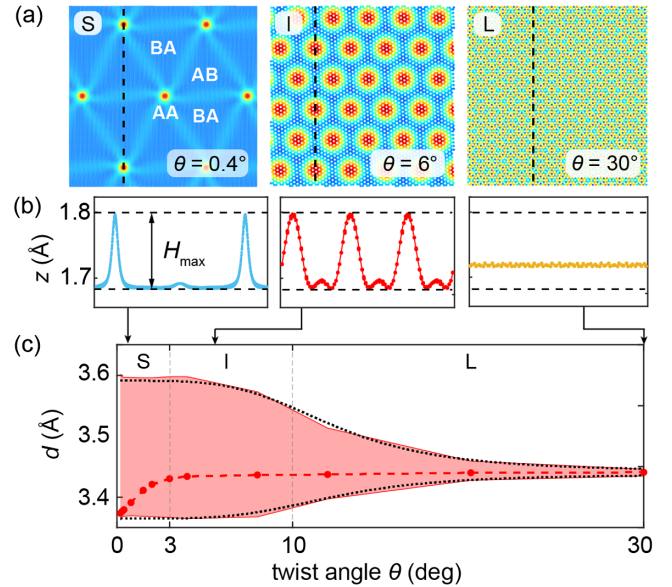


FIG. 3. (a) Out-of-plane  $z$  distance (corrugation) of a single TBG layer from the midinterface plane, fully relaxed at  $T = 0$  K for  $S$ ,  $I$ , and  $L$  regimes. Red nodes mark large AA-like interlayer spacing, blue areas smaller AB-like spacing. (b) Corrugation profile along the dashed lines in (a). (c) Average (red dashed line) and minimum and maximum (pink-shaded region) relaxed interlayer spacing as a function of the twist angle  $\theta$ . The black dotted lines mark the analytical prediction of Eq. (3). The data were obtained as described in Sec. III.

from the sinusoidal shape. It consists of a sequence of narrowly peaked, well-spaced misfit dislocations, or discommensurations (McMillan, 1976) of a constant  $z$  magnitude, separating nearly  $AB$  and  $BA$  commensurate domains. The twist regime  $I$ , roughly from  $10^\circ$  to about  $3^\circ$  in TBG, is intermediate, the corrugation growth is less pronounced, and the shape deviates from sinusoidal. These different regimes and crossovers were encountered in many previous studies and simulations (Bohlein, Mikhael, and Bechinger, 2012; Kim *et al.*, 2012; Alden *et al.*, 2013; Uchida *et al.*, 2014; Woods *et al.*, 2014; Berman *et al.*, 2015; Jain, Jurićić, and Barkema, 2016; Yoo *et al.*, 2019; Maity *et al.*, 2020; Weston *et al.*, 2020; Kazmierczak *et al.*, 2021; Zhang *et al.*, 2022), where some aspects were described. These twist-dependent structural differences also imply different frictional properties, a seldom addressed aspect that plays an important role in our discussion. As prototypes of the two extreme limits  $L$  and  $S$ , we use  $\theta = 30^\circ$  [ignoring its special “quasi-incommensurate” geometry (Stampfli, 1986; Koren and Duerig, 2016b)] and  $\theta = 2^\circ$  here, respectively. Smaller twist angles with moiré size growing as  $\theta^{-1}$  for  $a = b$  [Eq. (1)] are computationally more expensive and therefore harder to explore. This problem does not arise in heterostructures, where  $a \neq b$  and by Eq. (1) the moiré size  $\lambda$  remains finite at  $\theta = 0$ . That is illustrated for  $h$ -BN/graphene in Fig. 4(a).

### B. Understanding the relaxed structural regimes

A good analytical understanding of the upper and lower envelopes of the shaded zone in Fig. 3(c),  $d_{\text{upper}} = d_0 + 4H/3$

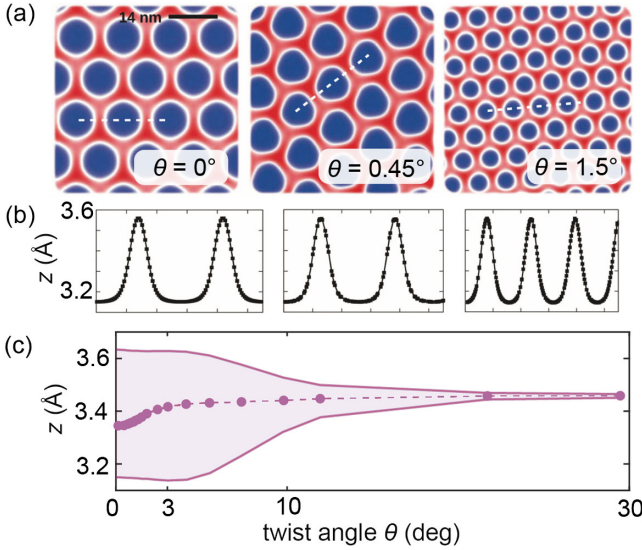


FIG. 4. Out-of-plane moiré corrugation for graphene/*h*-BN simulated heterostructures at various twist angles:  $\theta = 0^\circ$ ,  $0.45^\circ$ , and  $1.5^\circ$ . (a) The moiré pattern and (b) the out-of-plane corrugation magnitude along the white dashed traces in (a). (c) Maximum, minimum, and average values of the  $z$  coordinate of carbon atoms in the upper graphene layer over the flat *h*-BN substrate as a function of misalignment angle. Adapted from Guerra *et al.*, 2017.

and  $d_{\text{lower}} = d_0 - 2H/3$ , is given by the monolayer out-of-plane corrugation magnitude

$$H(\theta) = \frac{\alpha U_0 \lambda^4(\theta)}{32\pi^4 \alpha^2 D d_0 / 3\sqrt{3}(1-\nu^2) + k_z d_0 / 2 + 144\epsilon \lambda^4(\theta) / d_0}, \quad (3)$$

where  $\lambda(\theta)$  is the moiré size at the twist angle  $\theta$  [Eq. (1)],  $U_0$  is the energy barrier against sliding at the interlayer equilibrium distance  $d = d_0$ ,  $\alpha$  describes the decay rate of  $U_0(d)$ ,  $\epsilon$  is the adhesive energy per atom in the perfect *AB* stacked bilayer, and  $D$  and  $\nu$  are the bending stiffness and Poisson's ratio of monolayer graphene. Moreover,  $k_z$  is an effective interatomic stiffness, qualitatively representing the rigidity of the semi-infinite bulk supporting the bilayer interface. The Lennard-Jones parameters  $\epsilon$  and  $d_0$  generically describe the  $z$ -dependent interlayer adhesion energy, which is assumed to be weakly  $(x, y)$  sinusoidally dependent (Wang, Ma, and Tosatti, 2023). Its transparent contents is that the out-of-plane corrugation originates from the in-plane energy barrier  $U_0$ , hindered by both bending stiffness  $D$  and adhesion  $\epsilon$ . Because Eq. (3) assumes a weak out-of-plane corrugation, it applies only to  $L$  and part of the  $I$  regime, where the local interlayer spacing is still above its minimum  $d_{AB}$  and below its maximum  $d_{AA}$  of bulk graphite. When TBG is “encapsulated” between supports (described in Sec. III), that regime is realized for  $\theta \geq 5^\circ$ . For smaller twist angles, regime  $S$ ,  $\min(z)$  approaches  $z_{AB}$  and  $\max(z)$  approaches  $z_{AA}$  such that  $H_{\text{max}} = z_{AA} - z_{AB}$ , as shown in Fig. 3(b). The range of interlayer spacing is shown as a shaded zone in Fig. 3(c). In the graphene bilayer, the maximum width reached by the

pink zone ( $\sim 0.2 \text{ \AA}$ ) corresponds to the excess interlayer distance of the *AA* metastable stacking relative to that in the stable *AB* stacking. The globally flat bilayer is symmetrically moiré corrugated with magnitude  $2H$ , where  $H$  describes the single layer corrugation. In heterobilayers the corrugation is asymmetrical, but the overall behavior under twist is similar. For example, in the flexible-graphene/rigid-*h*-BN depiction in Figs. 4(a) and 4(b), the variable twist angle gives rise to a similar broadening of the interlayer distance [Fig. 4(c)].

### III. TWISTED GRAPHENE INTERFACE SIMULATIONS: A DEMONSTRATION TOOL

Here we describe the simulated systems that we use for demonstration and discussion. They are two representative model setups, sketched in Fig. 5, of 2D graphitic homostructure interfaces, as well as graphene/*h*-BN heterostructure interfaces. For all simulations, the box size is relaxed at the beginning to set the in-plane stresses  $p_{xx}$  and  $p_{yy}$  to zero. All molecular dynamics (MD) simulations used the LAMMPS code (Plimpton, 1995; Thompson *et al.*, 2022). The interlayer and intralayer interactions of graphene layers are described by the registry-dependent interlayer potential (Leven *et al.*, 2016; Ouyang *et al.*, 2018) and the second-generation reactive empirical bond order potential (Stuart, Tutein, and Harrison, 2000; Brenner *et al.*, 2002), respectively. Optimized for high pressure conditions (Ouyang *et al.*, 2020), the former is meant to reproduce the sliding energy barrier and the binding energy of 2D materials, while the latter describes the mechanical behavior of graphene well (Rowe *et al.*, 2018). A Langevin thermostat at temperature  $T$  is applied to the lowest substrate layer in each of the configurations of Fig. 5.

*Open boundary conditions: A sliding island.* The first setup [Figs. 5(a) and 5(c)] is, when idealizing some experimental systems, a finite-size graphene flake in the form of a circular island (blue), sliding over an infinite, PBC graphene substrate (red). For simulations, the model is composed of four layers of 2D material. The two lower layers represent the “substrate,” whereas the two upper layers represent the the slider. This open boundary conditions (OBC) setup allows an arbitrary twist angle and arbitrary incommensurability of in-plane lattice spacing for heterostructure interfaces. The island edge breaks translational invariance. An issue is the spontaneous torque, which is generally nonzero and pushes the twist angle  $\theta$  toward energetically favorable alignments such as  $\theta = 0$ . To prevent this in simulations the overall twist  $\theta$  is kept strictly constant by setting the overall angular momentum to zero at all times. In a homostructure interface such as a TBG, the torque gets negative and large at smaller twist angles, where the island tends to rotate toward  $\theta = 0$ . While for a mesoscopic or macroscopic island this negative torque may not really succeed in producing a rotation, in microscopic islands it surely can, and that poses an obstacle to the study of twist angle dependence of all frictional properties. This spontaneous rotation occurs not only in homojunctions (Filippov *et al.*, 2008) but also in heterojunctions (D. Wang *et al.*, 2016).

*Periodic boundary conditions: A perfect infinite interface.* The second model pictured in Figs. 5(b) and 5(d) is an

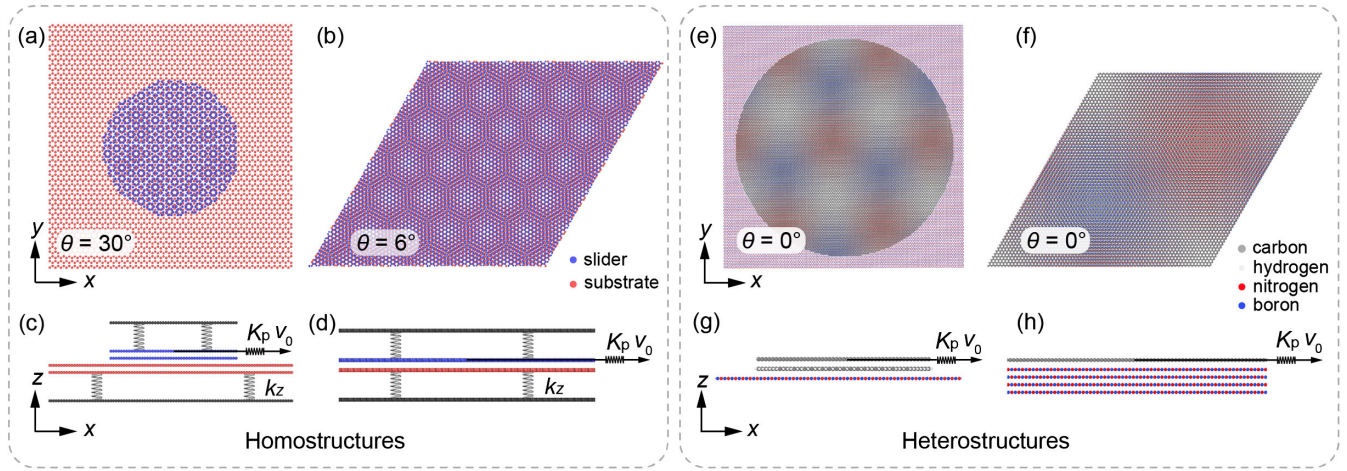


FIG. 5. Top and side views of prototypical nanofriction setups. (a) Circular island, OBC bilayer interface. (b) Boundary-free PBC bilayer interface. Note the differing moiré patterns of the  $30^\circ$  and  $6^\circ$  twist angles, respectively. (c),(d) Side view of two configurations. The slider and substrate layers are shown in blue (upper center) and red (lower center); the encapsulating stages (top and bottom layers) are black, with their vertical grip mimicked by springs  $k_z$ . The slider's center of mass is pulled with velocity  $v_0$ , through a spring  $K_p$  representing the overall effective stiffness of the pulling system. (e)–(h) Sliding configurations for graphene/*h*-BN heterostructures in the literature (Song *et al.*, 2018; Mandelli *et al.*, 2019; Wang, Cao *et al.*, 2019).

infinite supported graphene/graphene interface with fully periodic boundary conditions (PBC). A discrete series of twist angles ranging from  $0.1^\circ$  to  $30^\circ$  are constructed by means of artificially commensurate periodic supercells (Trambly de Laissardière, Mayou, and Magaud, 2010). There are no edges or defects, making the model suitable for the study of delicate structural superlubricity questions at small twist angles. The residual commensurability energy barrier is irrelevant at sufficiently large system sizes. A more serious drawback in this case is that by necessity the cell size depends upon the twist angle [Eq. (1)], which complicates comparisons between different twists. At small twist angles, the homostructure moiré and thus the simulation size become large. Thus, in PBC we limit the number of 2D layers, which are still supported by the  $k_z$  vertical springs, to two; there are no extra encapsulating layers.

*Twist-dependent energy and torque.* Structural optimization of the aforementioned models provides qualitative and quantitative information reflecting the different regimes. They are shown in Fig. 6 for a graphene/graphene interface. The main regime is the energy/atom interface relative to that of the commensurate Bernal *AB* stacking  $\Delta E = [E_{\text{interlayer}}(\theta) - E_{\text{interlayer}}(0)]/N$ , where  $N$  is the total number of atoms in the upper (or lower) layer at the interface. Another is the torque, the  $z$  component of  $\mathbf{Q} = (\sum_i^N \mathbf{r}_i \times \mathbf{F}_i)/N$ , where  $\mathbf{r}_i$  and  $\mathbf{F}_i$  are the position (relative to the slider's center of mass) and force of the  $i$ th slider atom. From energy, the torque magnitude is obtained as  $|\mathbf{Q}| = -d\Delta E/d\theta$  and is extracted, respectively, from the island and PBC simulations (Fig. 6). With the present force field the interface interaction energy (adhesive and thus negative) evolves from constant and  $-44.7$  meV/atom in the large incommensurability regime  $L$  to  $\sim -48.7$  meV/atom at  $\theta = 0$  in full commensurate *AB* stacking, and thus with  $N\Delta E/E_{\text{interlayer}}(0) \approx 9\%$ . The interaction energy and also the average interlayer spacing [the red dashed line in Fig. 3(c)] actually appear to indicate only two

regimes, i.e.,  $L + I$  and  $S$ . Evidence of a separate intermediate regime  $I$  between  $L$  and  $S$  is provided by the onset of a torque pushing monotonically toward  $\theta = 0$ . This coincides with the beginning of regime  $S$ , where upon decreasing twist there is a leveling off of the corrugation magnitude  $H_{\text{max}} = z_{AA} - z_{AB}$ .

*Extracting static and kinetic friction.* All layers [four in the island case in Fig. 5(c) and two in the infinite case in Fig. 5(d)] are mechanically flexible, with atoms in the upper layer of the slider and the lower layer of the substrate connected to rigid planes [the black encapsulating stage in Fig. 5(c)] through  $z$  harmonic springs  $k_z = 2.7$  N/m, the elastic modulus of graphite<sup>1</sup> (Liu, Liu *et al.*, 2012; Wang, Qu *et al.*, 2019). The center of mass (c.m.) of the slider's upper layer is connected to a virtual stage through the pulling spring with stiffness  $K_p$ , which represents the effective lateral stiffness of the pulling system. In NEMD simulations, the stage moves along the  $x$  direction with a constant velocity  $v_0$ .

The static friction  $F_s$ , the smallest force required to initiate sliding, is calculated using quasistatic protocols (Bonelli *et al.*, 2009; Mandelli *et al.*, 2017). Simulations with  $\theta$  smaller than  $1^\circ$  contain one moiré, while systems with larger twist angles afford multiple moirés [Fig. 5(b)]. The kinetic friction  $F_k$  is the average force necessary to maintain steady-state sliding with an average velocity  $v$ . It characterizes the average energy dissipation during sliding. It is calculated as  $F_k = \langle K_p(v_0 t - X_{\text{c.m.}}) \rangle$ , where  $X_{\text{c.m.}}$  is the c.m. position of the slider and  $\langle \dots \rangle$  denotes the long time average over a steady sliding state. To address correlations between friction and contact area  $A$ , temperature  $T$ , sliding velocity  $v$ , and normal load  $F_N$ , we control these variables and adjust the circular slider

<sup>1</sup>This is an extreme value mimicking a rigid encasing. An alternative value for a twisted graphite interface could be (Wang, Ma, and Tosatti, 2023)  $\sim 0.1$  N/m, which is much smaller. The actual magnitude of  $k_z$  has little effect on the moiré corrugation  $H$ .

diameter  $D$ , the stage velocity  $v_0$ , and the thermostat  $T$ . Load is controlled by keeping the rigid bottom plane fixed and positioning the top rigid plane at variable  $z$ . Compared to the method of directly applying a uniform normal force to each slider atom, this method is more realistic, allowing the slider atoms to adaptively experience a nonuniform normal force.

#### IV. SIMULATED 2D SLIDING FRICTION

The previously described model setups provide typical energy and friction data that can be used for the discussion of sliding in 2D materials.

##### A. Static friction and energy barriers

The total potential energy, the sum of intralayer and interlayer contributions, depends on the relative lateral coordinate of the two facing layers. The potential energy and the sliding energy barriers for MD simulations can be generated by means of well tested empirical force fields. Force fields are adequate as long as bond breaking and bond formation does not occur, as we assume to be the case in the sliding of 2D materials. First-principles calculations were also carried out (Reguzzoni *et al.*, 2012; Righi, 2021). However, they are difficult to extend to large simulation cells, which are essential for the present problems. Starting with first-principles calculations, force fields were even parametrized so as to preserve

the same high precision but better efficiency in that respect (Leven *et al.*, 2014, 2016; Wen *et al.*, 2018; Ouyang, Hod, and Guerra, 2021).

The periodic moiré corrugation is depicted in Fig. 6(a) for the island (OBC) case and in Fig. 6(d) for the infinite bilayer (PBC) case. The AA regions stand out for their higher interlayer distance and weaker interlayer attraction, while the AB and BA regions indicate the opposite. The AB-BA dislocation network joining the AA nodes is visible in the small twist angle cases in Fig. 6(d). The twist concentrates to a local rotation angle of the AA nodes in regime  $S$  [visible in Fig. 6(d)], as noted earlier (Angeli *et al.*, 2018; Zhang and Tadmor, 2018). The average interlayer energy of Fig. 6(b) evolves from constant  $L$ -regime incommensurability  $\theta > 10^\circ$ , dropping toward the commensurate value with the asymptotic power law  $\Delta E \propto \theta$  in the  $S$  regime  $\theta \ll 3^\circ$ . For the PBC structural superlubric case [Fig. 6(e)], the prefactor is 1.43 meV. At the same time, a torque arises in the regime pushing toward  $\theta = 0$ ; see Figs. 6(c) and 6(f). The energy evolution upon static sliding is instructive. To begin, the total energy in the perfectly incommensurate infinite bilayer should be strictly constant, regardless of the relative position of the two layers. For a finite-size slider, however, the energy depends on the position, with barriers that depend on the size and sliding direction. This is exemplified in the right panel of Fig. 6(b) for a circular island, where the energy oscillations correspond to moiré cells entering or exiting the

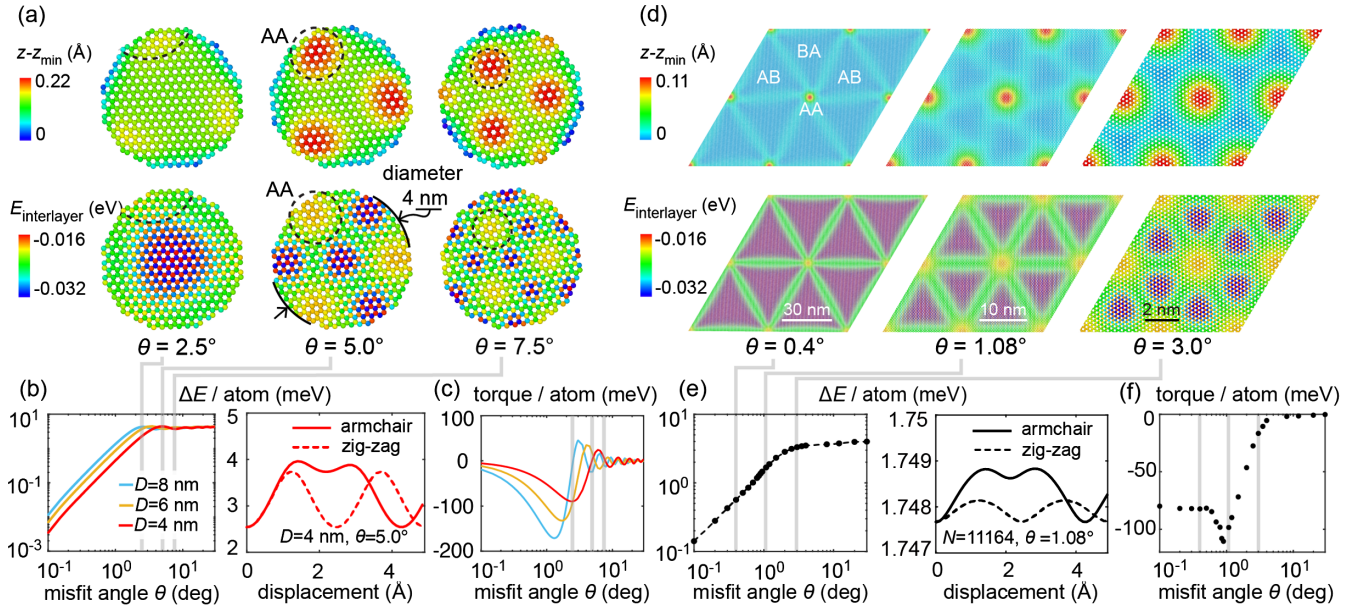


FIG. 6. Moiré corrugation patterns, energy, and rotational torque of the OBC (island) and PBC (infinite) graphene/graphene interfaces. (a)  $z$  coordinates (upper panels) and per-atom interlayer interaction  $E_{\text{interlayer}}$  (lower panels) for circular islands with diameter  $D = 4$  nm and twist angle  $\theta = 2.5^\circ, 5.0^\circ$ , and  $7.5^\circ$ . (b) Per-atom interlayer interaction energy difference  $\Delta E$  relative to perfect AB stacking for islands with different diameters as a function of twist angle (left panel), and for one moving island as a function of displacement along the substrate armchair (vertical) and zigzag directions (horizontal), with the periodicities  $\sqrt{3}a = 4.26$  Å and  $a = 2.46$  Å, respectively. (c) Per-atom rotational torque of graphene islands with different radii. The three red vertical lines in (b) and (c) correspond to the twist angles shown in (a): the rotationally most unstable angle and the two locally stable angles (zero torque). (d) The same plots as in (a) for PBC infinite interfaces with twist angles  $\theta = 0.4^\circ, 1.08^\circ$ , and  $3.0^\circ$ . (e) The same as (b) for PBC. The three gray vertical lines in (e) and (f) correspond to the twist angles shown in (d). By comparing the OBC island with PBC energy against the slider position, one can note the direction-dependent energy barriers. Despite the apparent similarity, the large island barriers are real, whereas the small PBC barriers are an artifact due to the finite cell. In addition, the OBC torque oscillations are real features of the island edge interfering with the moiré. The torque minimum near  $1^\circ$  signals a change of misfit regime from independent to dependent on elasticity (see the text).

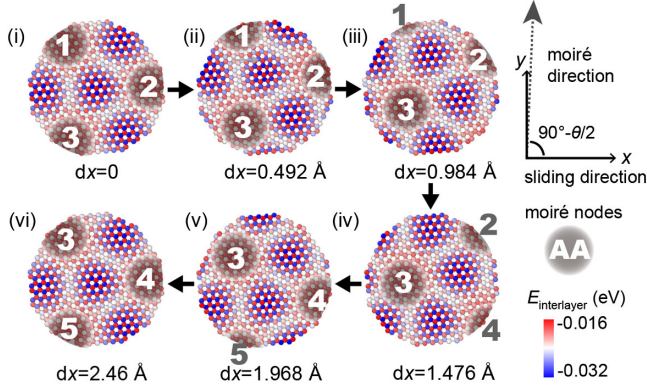


FIG. 7. Evolution of an interlayer energy map during sliding by  $dx$  along  $x$  of a circular island with a diameter of 4 nm and a twist angle  $\theta = 5^\circ$ . Three AA nodes near the edge in (i) are highlighted and tracked as they move. When they cross the edges, the interlayer energy develops a barrier.

perimeter edge. For curiosity, we also show the energy barrier of the PBC case of Fig. 6(e), which is completely artificial and utterly negligible.

To clarify the origin of the frictional barrier in OBC systems, Fig. 7 shows the evolution of the moiré pattern (via energy distribution) as an island slides. Two aspects emerge. First, as the island slides along  $(1, 0)$  with velocity  $v$ , the moiré pattern moves along  $(\sin(\theta/2), \cos(\theta/2))$  with a velocity  $v_M(\theta) = \lambda(\theta)v/a$ . Second, the manner in which this moving moiré hits the island edge is responsible for the sliding energy barrier [the middle panel of Fig. 6(b)]. Every time one or more of the AA nodes in the moiré cross inward or outward the edge (Fig. 7), the total energy undergoes a local maximum because local AA stacking costs about 15 meV/atom more than AB stacking (Popov *et al.*, 2012; Tan *et al.*, 2012; Wen *et al.*, 2018).

The reluctance of the island to admit or expel AA moiré nodes generates the barriers that cause the static friction against the incommensurate island motion. The evolution of this edge-induced barrier with island radius, its direct connection with uncompensated moiré cells, and the approximate description of its oscillatory and progressively decreasing impact on friction have been repeatedly emphasized in different contexts (Varini *et al.*, 2015; Koren and Duerig, 2016a; Cao *et al.*, 2022). Theoretical modeling also led to these friction oscillations being expressed with the radius of a circular island in terms of sinusoidal fitting for kinetic friction (Wang, Cao *et al.*, 2019; Wang, Qu *et al.*, 2019) and of Bessel functions for the static friction of rigid colloidal flakes (Cao *et al.*, 2022).

## B. Kinetic friction: Surfing moiré

Typical room temperature simulated force traces (whose steady-state average yields the kinetic friction  $F_k$ ) are shown in Figs. 8(a)–8(c) for PBC and OBC graphene contacts. In addition to homojunctions, force traces for PBC and OBC graphene/*h*-BN heterojunctions from the existing literature (Mandelli *et al.*, 2019; Wang, Cao *et al.*, 2019) are reproduced in Figs. 8(d)–8(f).

The PBC traces show a weak oscillation, and a sharply increasing mean value of friction as the twist angle decreases across from  $L$  regime at  $\theta = 30^\circ$  to  $I$  and  $S$ , eventually close to  $\theta = 0^\circ$ . The rise of friction reflects the decrease of interface mobility upon rise of the moiré size  $\lambda$  [Eq. (1)]. This reduces the density of AB-BA dislocations and changes their appearance from diffuse to localized, as shown in Figs. 3(a) and 6(d). The twist angle decrease also entails the rise of moiré velocity ( $|v_M| = v_0\lambda/a$ ) along a direction that is increasingly close to orthogonal to the sliding force [Eq. (2)].

The stiffness of the dragging spring is adjusted in simulations to scale as the number of slider atom  $N$  as  $K_p = Nk_i$ , where  $k_i = 0.1$  N/m, which keeps their frequency roughly constant. The transient inertial oscillation is a mere damping and parameter-dependent artifact and is of little further significance. The relevant information is the final parameter-independent steady-state friction; see Fig. 8(a).

Based on the reasonable assumption that dissipation comes mostly from out-of-plane motion of the atoms, the kinetic friction per atom of PBC superlubric sliding at  $T = 0$  K is analytically derived as (Wang, Ma, and Tosatti, 2023)

$$F_k = cm\zeta v_0 \left[ \frac{H(\theta)}{a} \right]^2, \quad (4)$$

where  $H$  is the out-of-plane corrugation,  $m$  is the mass per atom,  $v_0$  is the sliding velocity,  $a$  is the lattice spacing of the substrate, and  $c$  is a geometrical prefactor that depends on the twist angle and sliding direction, in our case  $c = (32/81)\pi^2$ . The phenomenological damping  $\zeta$ , a simulation parameter mimicking phonon dissipation in the supporting layers (Benassi *et al.*, 2010), is empirically set here in the ps<sup>-1</sup> range. Substituting  $H$  of Eq. (3), good agreement is obtained between this theoretically obtained friction and the simulation results; see Fig. 9. The linear size and velocity dependence of kinetic friction suggested by Eq. (4) also agrees with the simulations (Brilliantov *et al.*, 2023; Wang, Ma, and Tosatti, 2023). This indicates that the kinetic friction is negligible once velocity is scaled down from the m/s scale (typical of MD simulations) to experimental scales of  $\mu\text{m/s}$  or nm/s.

Kinetic friction is also controlled, unlike static friction, by the stiffness of the dragging spring  $K_p$  and the effective damping present in the system. For the OBC island with  $\theta = 30^\circ$ , for example, the pulling force for stiff or soft springs is sinusoidal or sawtooth, respectively [Fig. 8(b)]. This corresponds to the absence or presence of a mechanical instability: the latter is a necessary condition for stick-slip friction.

Discarding all twist angles at which the contact between the two layers is commensurate, we can ask whether there might be a single parameter that determines whether an island whose c.m. is pulled at low speed and small damping will slide smoothly or through mechanical instabilities. At  $T = 0$ , this amounts to a simple question of statics. When the magnitude of the slider's c.m. displacement  $\vec{R} = (X, Y)$  is increased adiabatically, the static evolution of the contact can occur either smoothly or through instabilities. In the paradigmatic 1D Prandtl-Tomlinson (PT) model (Prandtl, 1928; Tomlinson, 1929), the outcome is determined by competition between the energy barrier  $U_0$  and the effective lateral stiffness  $K_p$  (Vanossi *et al.*, 2013). When the dimensionless parameter



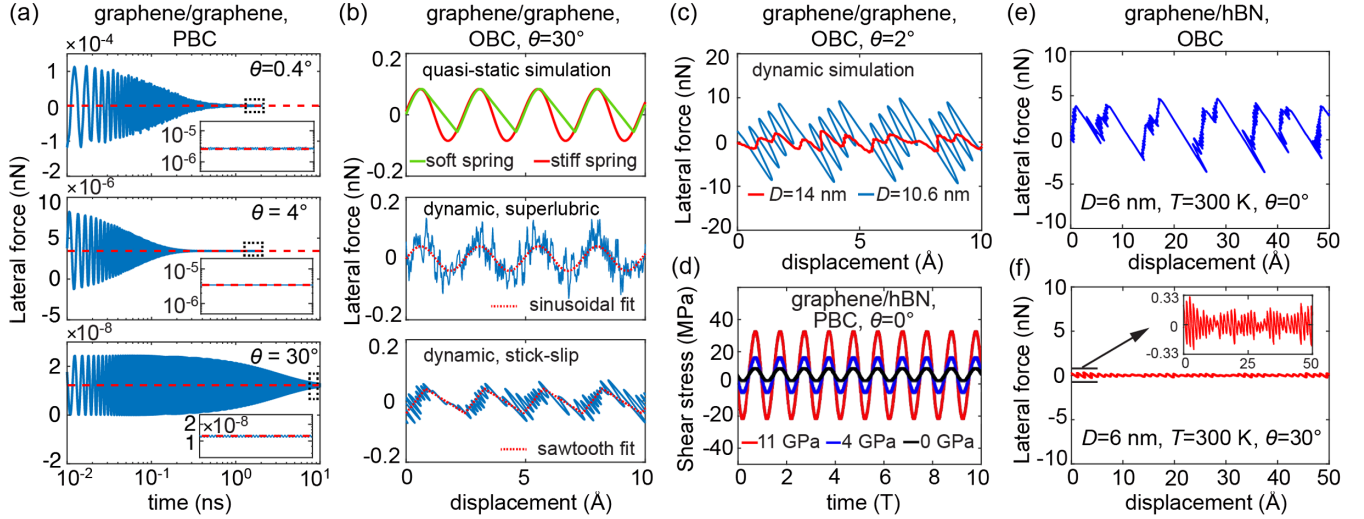


FIG. 8. Kinetic friction traces from (a)–(c) our simulations and (d)–(f) published simulation studies. The underlying static friction  $F_s$  is zero in PBC, signaling essentially perfect structural superlubricity, but nonzero in OBC, where pinning is due to the island edges. The kinetic friction  $F_k$  is the average lateral force. The friction force of PBC systems is normalized per slider atom and can be converted to the shear stress  $\tau = F/A_C$  by dividing the per-atom area of a carbon atom:  $A_C = \sqrt{3}a_{Gr}^2/4$ . (a) Frictional transient and convergence of PBC graphene-graphene contacts evolving in time ( $v_0 = 10$  m/s,  $T = 0$  K). The effective lateral stiffness  $K_p$  is adjusted case by case in order to keep the underdamped inertial oscillation  $\omega = \sqrt{K_p/M}$ , with  $M = Nm_C$  the slider mass within reasonable range. The mean friction (the red dashed line; magnified in the insets), here proportional to velocity, increases as the twist angle decreases, reflecting the severe mobility drop from the  $L$  to  $I$  to  $S$  regimes (the slider atom numbers  $N$  are 11 644, 6542, and 40 838 for  $\theta = 30^\circ$ ,  $4^\circ$ , and  $0.4^\circ$ , respectively). (b) Friction force of OBC graphene-graphene island of diameter  $D = 4$  nm with a twist angle  $\theta = 30^\circ$  as a function of the sliding distance. Upper panel: adiabatic protocol with stiff and soft pulling springs  $K_p = 100$  and  $1$  N/m, respectively. Lower panels: dynamic sliding simulations ( $v_0 = 10$  m/s,  $T = 298$  K) and the same spring stiffness: stiff and soft, respectively. Note the evolution from smooth sliding to stick-slip upon softening. (c) OBC friction force at a small twist angle of  $2^\circ$ . Blue and red represent the island diameters  $D = 10.6$  and  $14$  nm, respectively. Note the evolution from stick-slip at a small size, where edge pinning dominates, to a larger size, where the edge effect disappears. (d) Time evolution of shear stress (per-area friction force) in aligned graphene/h-BN heterojunctions under different normal pressures. The time unit is  $\sim 25$  ps. The incommensurability of the two lattices and the absence of edges in PBC predicts smooth sliding in this case too. Adapted from Mandelli *et al.*, 2019. (e),(f) Friction force of graphene/h-BN island contacts (OBC) for  $0^\circ$  and  $30^\circ$  twist angles (Wang, Cao *et al.*, 2019). The evolution from (e) stick-slip to (f) smooth sliding is associated with a dramatic shrinking of the moiré cell size with increasing twist.

$$\eta = \frac{2\pi^2 U_0}{K_p a^2} \quad (5)$$

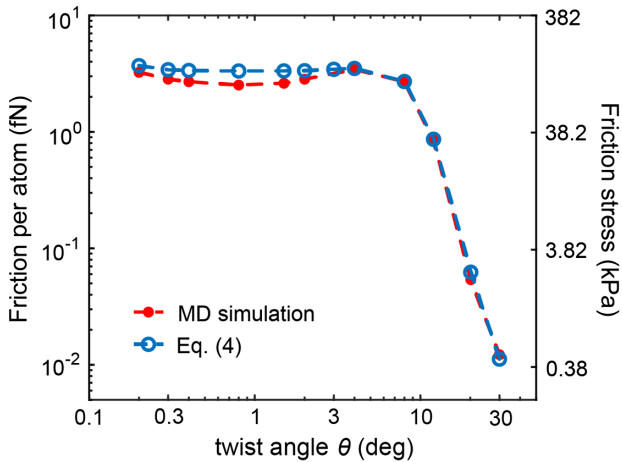


FIG. 9. Dependence of per-atom kinetic friction on the twist angle, where the red dots and blue circles represent the simulation results and theoretical results estimated from Eq. (4). The parameters used here are  $\zeta = 2$  ps $^{-1}$  and  $v_0 = 10$  m/s.

is smaller than 1, the evolution is smooth; when it is larger than 1, there is instability. Mechanical instability in turn leads to stick-slip motion at low velocities, small damping, and low temperatures.

This concept can be extended to 2D material sliding interfaces. Assuming a fixed twist angle adequate for large islands, the single c.m. coordinate's step-by-step static evolution controls all other internal coordinates. The internal coordinates follow adiabatically owing to energy-minimizing relaxation at each step. Thus, we can generally describe the adiabatic sliding of a uniformly pulled island as that of a single effective “particle” whose coordinate  $\vec{R}$  is that of the c.m., and whose potential energy is the total energy  $E(\vec{R})$ .

This permits the use of a PT-like parameter  $\eta$  to be extended heuristically to a sliding island or flake once the three quantities involved  $U_0$ ,  $a$ , and  $K_p$  are properly interpreted and replaced with the effective quantities  $U_{\text{eff}}$ ,  $a_{\text{eff}}$ , and  $K_{\text{eff}}$  (Wang, Vanossi, and Tosatti, 2024).

To illustrate and assess how this works, consider an incommensurate island of twist angle  $\theta$  and diameter  $D$  moving along the zigzag direction  $X$  in Fig. 6(b), middle panel. Starting with the minimum at  $X = 0$ , the adiabatic total energy  $E(X)$ , which is close to sinusoidal for rigid layers, will still be periodic with the same period  $a$  after full relaxation is allowed at the increasing c.m. coordinate  $X$ . The effective barrier maximum  $U_{\text{eff}} = E(a/2) - E(0)$  is determined by relaxation, essentially taking place near the pinning center (here the edge). After relaxation, the “effective lattice spacing”  $a_{\text{eff}} = 4X_{\text{inst}}$ , where the c.m. coordinate  $X_{\text{inst}}$  of the mechanical instability is the point of maximum slope  $dE/dX|_{X=X_{\text{inst}}} = \max$ . The deformability of the island, both in plane and out of plane, causes the relaxed  $E(X)$  to decrease compared to the rigid one at all  $X$  and to deviate from sinusoidal. In our case, we find that the relaxed  $X_{\text{inst}}$  grows slightly larger than  $a/4$ , yet still smaller than  $a/2$ . This result is more general than the case in point. As can be seen in Fig. 6(b) for the zigzag and armchair directions, the maximum slope coordinates  $X_{\text{inst}}$  (i.e.,  $a_{\text{eff}}$ ) are not much different. This conclusion is actually not limited to these two directions (Wang, Vanossi, and Tosatti, 2024). Next one finds that the energy barrier  $U_{\text{eff}}$  also differs modestly from the rigid one. Finally, the effective lateral stiffness  $K_{\text{eff}}$  must generally include that of the island’s interior  $k_{\text{isl}}$ , for example, in the linear form  $K_{\text{eff}}^{-1} = k_{\text{isl}}^{-1} + K_{\text{p}}^{-1}$ . As detailed in Sec. VIII, the intraisland stiffness  $k_{\text{isl}}$  is usually larger than the external stiffness  $K_{\text{p}}$ ; thus,  $K_{\text{eff}}$  may often be approximated by  $K_{\text{p}}$ .

With these qualifications, the PT-like parameter  $\eta$  of Eq. (5) can still be used to identify and understand the sliding regime of 2D islands and flakes (Wang, Vanossi, and Tosatti, 2024). In particular, as the size grows,  $a_{\text{eff}}$  remains stable while  $U_{\text{eff}}$  grows with size. Therefore, unless  $K_{\text{p}}$  is also raised, the  $\eta$  of Eq. (5) will inevitably grow larger than 1. Thus, at a fixed pulling spring stiffness, the mechanical instability will be the rule above a certain island diameter, a point also subsequently addressed in greater detail. The qualitative gist of Eq. (5) is thus that smooth sliding remains restricted to sufficiently small islands and sufficiently stiff pulling springs.

## V. AREA DEPENDENCE

We can now discuss the friction dependence upon the various parameters. We begin with the contact area  $A$  dependence of static and kinetic friction in a structurally lubric 2D interface. Kinetic friction is well defined for any system or condition; static friction is zero or undefined for a nanoscale system at a finite temperature  $T$ . Thermal fluctuations will always, after a sufficient time  $t_D(A, T)$ , overcome the pinning energy barriers and allow diffusion. This condition, sometimes called thermolubricity (Krylov and Frenken, 2014; Pellegrini *et al.*, 2019) and discussed later, permits smooth sliding of a nanosystem no matter how weak the applied force is. Considering that  $t_D$  grows with mass, and therefore with area, we generally assume in the present discussion of 2D interfaces that  $t_D$  is large enough that static friction can be defined and measured if it is present. Thermolubric conditions are more difficult to reach for large sliders whose low-temperature

friction is stick-slip. Force traces for different boundary conditions and different systems, including our prototype graphene-graphene simulated sliding, are presented in Figs. 10(a)–10(c) for both the static and kinetic friction of  $\theta = 2^\circ$  and  $\theta = 30^\circ$  systems.

To begin, consider static friction  $F_s$ , which originates from energy barriers that impede free sliding. In principle, in a simulated slider the energy barrier is always nonzero, both in the island OBC case and in the defect-free PBC case. Yet, in PBC the energy barrier is small and nonphysical, caused by the artificial high order commensurability introduced by the finite simulation cell. This barrier magnitude drops quickly with size, much faster than that of an island. As exemplified in one dimension (Theodorou and Rice, 1978), if the simulation cell size is (in this case in the direction of sliding)  $p$  times larger than that of the moiré cell, of order  $\lambda$ , then the PBC barrier is qualitatively expected to drop like  $\exp(-p)$ . That is, in our case like  $\exp(-N^\beta)$ , with  $0 < \beta < 1/2$ . This ready disappearance of size effects is the standard reason why PBC are generally chosen to approach infinite defect-free systems. In defect-free PBC simulations of 2D incommensurate materials, the static friction is generally undetectable for most sizes: a circumstance that allows structural superlubric conditions to be explored, at least theoretically.

Static friction of incommensurate interfaces is associated with defects that break the perfect translational invariance of potential energy [barring here the possibility of Aubry pinning (Peyrard and Aubry, 1983)]. Let the defects occupy a fraction  $f(A) = \delta A/A$  of the total area  $A$ . Unless their number is itself proportional to  $A$ ,  $f$  will tend to zero in the large size limit, generally as  $f \sim A^{\alpha-1}$  with  $0 < \alpha < 1$ . The energy barrier and the corresponding static friction, entirely due to defects in a structurally lubric interface, should thus be at most proportional to  $f(A)$ . For an island of  $N$  atoms where  $A = \rho_{2D}N$  and  $\rho_{2D}$  is the 2D atom density, the edge is the omnipresent minimal defect. The energy barrier and the corresponding static friction can in this case vary with increasing size at most as  $N_{\text{edge}}/N \sim N^{\alpha-1}$  with  $\alpha = 1/2$ . However, not all edge regions are equally efficient in producing barriers. The simulated OBC static friction of  $\theta = 30^\circ$  [the green squares in Fig. 10(a)] has an area dependence  $F_s \propto A^{1/4}$ , showing that the circular island edge is, thanks to its smoothness, a relatively mild pinning defect. The simulated sublinear static scaling results are compatible with existing studies (Koren and Duerig, 2016a; Sharp, Pastewka, and Robbins, 2016; Dietzel *et al.*, 2018).

The simulated area dependence of kinetic friction shown in Figs. 10(a)–10(c) is generally different than static friction. In the large area limit  $A \rightarrow \infty$ ,  $F_k$  is proportional to  $A$  itself for the defect-free, superlubric PBC case. Kinetic friction, however, is small and would hardly be measurable at low experimental velocities [Eq. (4)]. The OBC case is different. The edges give rise to a large kinetic friction that varies sublinearly with area. Owing to sublinearity, at sufficiently large areas and/or large speeds and large pulling stiffnesses the edge friction should become irrelevant, with a crossover to linear growth with area, as exemplified during our discussion of velocity dependence. That said, we conclude that edge and defect friction appear to be crucial and in fact dominant in

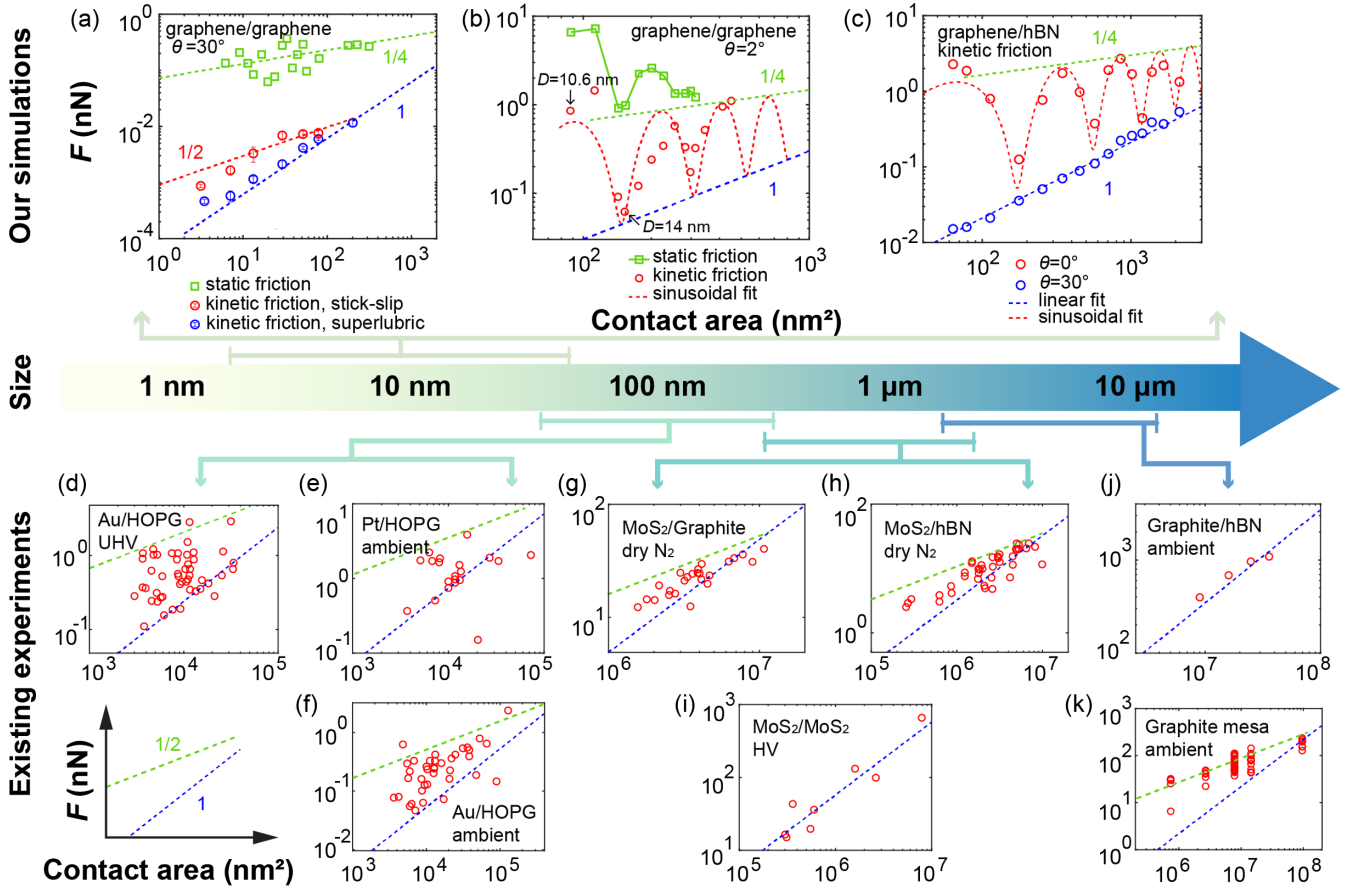


FIG. 10. Area dependence of nanoscale and mesoscale kinetic and static friction of 2D materials from simulations (upper panels) and experimental kinetic friction data (lower panels) across the scale. (a) Graphene-graphene contacts with a large twist angle  $\theta = 30^\circ$  ( $v_0 = 30$  m/s,  $T = 300$  K). The green and red data points represent the OBC circular island static friction and kinetic friction, and the blue data points indicate the superlubric regime kinetic friction (the static friction is zero). The green, blue, and red dashed lines are power-law fits  $F \sim A^\alpha$  with exponents 0.25, 0.5, and 1. (b) Graphene-graphene contacts with small twist angle  $2^\circ$  ( $v_0 = 10$  m/s,  $T = 300$  K). The green and red data points represent the static and kinetic friction of OBC islands, and the red dotted curve is the sinusoidal fitting whose oscillations reflect successive moiré entering and exiting the island (Wang, Cao *et al.*, 2019). Two typical cases are labeled, with diameters of 10.6 and 14 nm, respectively, at local friction maximum and minimum. (c) Graphene-hBN contacts with twist angle  $\theta = 30^\circ$  and  $0^\circ$  ( $v_0 = 10$  m/s,  $T = 300$  K). The red ( $\theta = 0^\circ$ ) and blue data points ( $\theta = 30^\circ$ ) represent the kinetic friction for the OBC graphene island [Fig. 5(e)]. Replotted with data from Wang, Cao *et al.* (2019). Comparing (b) and (c) with (a), note that the lowest friction values, where the edge does not contribute to friction, scale linearly with area, indicating structural superlubricity at all special island diameters of the sequence  $D_n = \sqrt{3}\lambda(n/2 + 1/8)$ , with the integer  $n \geq 2$ . The largest friction values, which are edge related, instead scale sublinearly, indicating proportionality to static friction (the red dashed upper envelopes). The scaling exponent 1/4 is particular to the circular shape. Most other shapes, possessing straight edge portions, scale with exponent 1/2. (d)–(k) Collection of 2D material kinetic friction data. The red circles represent data extracted and replotted from original papers (Dietzel *et al.*, 2013; Cihan *et al.*, 2016; Li *et al.*, 2017; Özoğul *et al.*, 2017; Wang, Cao *et al.*, 2019; Qu *et al.*, 2020; Liao *et al.*, 2022). The upper green dashed lines show sublinear scaling of the highest friction points. The lower blue dashed lines underline the linear scaling of the lowest friction points, which is analogous in experiments and simulations.

most experimental data, where velocity is low ( $\sim \mu\text{m/s}$ ) and pulling stiffness is generally small (of the order 10 N/m).

For the defect-free, sufficient large size system, the linear growth of kinetic friction with area is understood by considering that the frictional power  $P_{\text{ins}} = (1/\tau) \int_0^\tau F v dt$  must be dissipated roughly as

$$P_{\text{diss}} = \sum_{\alpha}^{x,y,z} \zeta_{\alpha} \sum_{i=1}^N m_i \langle v_{i,\alpha}^2 \rangle, \quad (6)$$

where  $\zeta_{\alpha}$  is the damping coefficient along the  $\alpha$  direction ( $\alpha = x, y, z$ ),  $m_i$  is the atomic mass, and  $v_{i,\alpha}$  is the velocity  $\alpha$  component of the interface atom  $i$ . The main source of atom velocity [a vector quantity whose most important dissipative component in 2D materials is out of plane (Song *et al.*, 2018; Mandelli *et al.*, 2019)] is the sliding-induced in-plane motion of the moiré pattern. Moiré solitons act here as quasiparticles moving in a viscous medium, dissipating energy proportionally to their velocity, which is in turn proportional to the sliding velocity. The moiré pattern (unlike the island edges)

occupies a fixed fraction of the total interfacial area  $A$ . Therefore, the defect-free superlubric friction caused by moiré motion grows proportionally to the area  $A$ .

The aforementioned conclusion, namely, that the area dependence of structurally lubric 2D kinetic friction differs from that of static friction, is valid for sufficiently large areas. In island sliders of small diameter, or other realistically defected systems where near-defect atoms are an important fraction, pinning is strong, and both static and kinetic friction grow sublinearly with area with the same power law, as they are indeed related and proportional. The island's edge-related energy barrier, demonstrated earlier, causes the stick-slip sliding at low velocity and for sufficiently soft pulling spring stiffness  $K_p$ .

In stick-slip sliding, the single contact force trace is sawtoothlike [Fig. 8(b)]. When the damping is sufficient, the average kinetic friction (the force-displacement area) is ruled by static friction (the sawtooth's maxima) and no longer by the moiré viscous translation, as in the superlubric case. As a result, both static friction and the corresponding stick-slip kinetic friction grow sublinearly with area. In Fig. 10(a), this regime is seen in the initial part of the island kinetic friction, where the edge-related stick-slip sliding dominates. Such low friction 2D interfaces are commonly encountered (Müser, Wenning, and Robbins, 2001; Dietzel *et al.*, 2013; Cihan *et al.*, 2016; Kawai *et al.*, 2016; Mandelli *et al.*, 2018; Ouyang *et al.*, 2018; Qu *et al.*, 2020). Even if stick-slip sliding is invisible in force traces, generally owing to cancellation among multiple contact regions, it must be present when the velocity dependence is less than linear. At the same time, the sublinear dependence of friction force on the contact area provides the signature of underlying structural superlubricity of the defect-free portions. In that sense it can be used instead of the more general definition of superlubricity in which friction coefficients are lower than 0.01 (Baykara, Vazirisereshk, and Martini, 2018; Martin and Erdemir, 2018).

*Static friction.* Direct static friction experimental values are rarely published because of poor reproducible statistics. Operatively, one could extract them as the maxima of frictional traces in cases where sliding is impeded by a single obstacle or barrier and stick-slip sawtooths are evident. In most cases, however, experimentally sliding interface sizes are large, with multibarriers, or asperities acting at the same time. Their interference, and the mesoscopic or macroscopic nature and stiffness of the sliding equipment, lead in most cases to the cancellation of stick-slip oscillations and sawtooths in the traces, which therefore appear smooth, even if they are noisy. (In principle, a Fourier transform of frictional noise could in the future be instructive in this respect.) As clarified in Sec. VI, the unmistakable earmark of stick-slip kinetics, implying in turn a nonzero static friction, is signaled by velocity dependence that is only weak or nil when friction is stick-slip.

*Kinetic friction.* Figures 10(d)–10(f) show friction results for the sliding of gold and platinum nanoparticles on highly orientated pyrolytic graphite (HOPG). There is a scatter of data, many with a substantially sublinear area dependence. The current understanding is that those growing sublinearly with  $\alpha \sim 1/2$  (Dietzel *et al.*, 2017) must do so owing to defects

whose density does not grow with area, most likely edge regions. Despite their apparently random spread, the log-log plot of data reveals that they all fall between two lines, one of slope  $\alpha = 1$  on the lowest friction side, the other with sublinear slopes  $\alpha \leq 1/2$ , as previously mentioned. The data scatter between the two lines can be given a suggestive interpretation, considering the size and shape of different sliding islands. Theory shows [see Figs. 10(b) and 10(c)] that circular islands of increasing radius should yield friction oscillating regularly between two straight lines that have different slopes, 1 and 1/4. Moreover, the shape-dependent exponent 1/4 appears to be an extreme value for the circular shape, above which it is easy, but below which it seems difficult to go. It is reasonable to expect that every new experimental data point to correspond to a random sequence with a different size and shape of the sliding islands, therefore falling between the two lines. If that were the case, one should actually expect aliasing, which is measurement of a regularly oscillating variable at random points. Dietzel *et al.* (2013) and Wang, Cao *et al.* (2019) discussed this problem. More insight could be obtained if and when friction force traces became available for sufficiently small size interfaces.

Another point for further inquiry is the apparently erratic value of the critical size where area scaling of the kinetic friction crosses over from sublinear to linear. For graphene-*h*-BN, experiments (Liao *et al.*, 2022) have shown that crossover occurs at around  $10^4$  nm<sup>2</sup>. This is consistent with a graphite-*h*-BN linear scaling at  $10^7$  nm<sup>2</sup> [Fig. 10(j)]. For the MoS<sub>2</sub>-*h*-BN and MoS<sub>2</sub>-graphite cases, the size scaling remains sublinear up to  $10^6$  nm<sup>2</sup> [Figs. 10(g) and 10(h)]. For graphite island-graphite contact, where edge friction dominates (Qu *et al.*, 2020), the sublinear scaling remains even up to  $10^8$  nm<sup>2</sup> [Fig. 10(k)]. There is a single-asperity theoretical estimate of the connection between critical velocity and area for that crossover. It is obtained by equating the slider's washboard frequency  $v/a$  to the characteristic oscillation frequency of the system inside the energy well  $(1/2\pi)\sqrt{(K_p + 2\pi^2 U_0/a^2)/M}$ . The resulting connection between stick-slip-ballistic crossover velocity and area is  $v_c = (1/2\pi)\sqrt{[K_p a^2(1 + \eta)]/\rho_{2D}A}$ , where the total mass  $M = \rho_{2D}A$  is proportional to the area  $A$ . Here  $\eta$  is the Prandtl-Tomlinson mechanical instability parameter [Eq. (5)], whereby stick-slip will only occur for  $\eta > 1$  (Vanossi *et al.*, 2013).

## VI. VELOCITY AND TEMPERATURE

After area, we discuss the dependence of friction on other parameters, starting with a closely related pair of variables: velocity and temperature. Before specializing to 2D material interfaces, it is useful to review the current generic understanding of nanoscale friction.

Stick-slip generally implies a weak logarithmic velocity dependence, roughly  $F_k \propto (\ln v)^\gamma$ , with  $2/3 < \gamma \leq 1$  (Gnecco *et al.*, 2000; Dudko *et al.*, 2002; Riedo *et al.*, 2003; Reimann and Evstigneev, 2004; Krylov *et al.*, 2005; Dong, Vadakkepat, and Martini, 2011; Müser, 2011). The well-known qualitative reason for this weak dependence is that

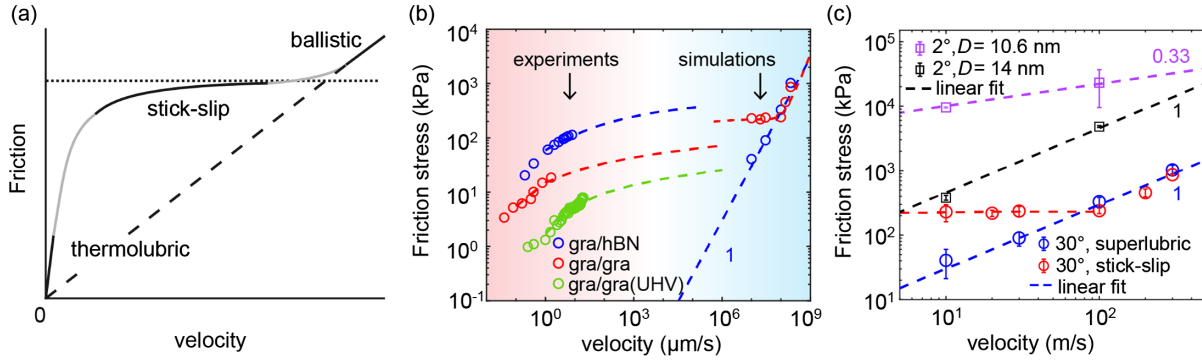


FIG. 11. Velocity dependence of kinetic friction of structurally lubricated contacts. (a) Three friction regimes of a pinned nanoslider as a function of velocity: thermolubric, stick-slip, and ballistic. From Krylov and Frenken, 2014. (b) A direction comparison between the experimental results (left pink region) and  $\theta = 30^\circ$  simulation results (right blue region). Circles within the low velocity range represent experimental kinetic friction data (Song *et al.*, 2018; Wang and Li, 2019; Liu *et al.*, 2020). The dashed lines are logarithmic fits. The MD simulation data and color are the same as in (c). The blue dashed (straight) line indicates linear (superlubric, thermolubric, or ballistic) friction scaling. Note the large velocity difference between simulations and experiments, whereby a high velocity ballistic regime is rarely reached in experiments and no low velocity thermolubric regime is reached in simulations. (c) Simulated kinetic friction in superlubric (blue circles,  $K_p = 100$  N/m) and stick-slip (red circles,  $K_p = 1$  N/m) sliding for large twist angle  $\theta = 30^\circ$ . For the larger stiffness the island friction is viscous in the entire range. The purple (black) squares display kinetic friction for small (large) island sizes at a small twist angle  $\theta = 2^\circ$ . All lines are power-law fits. Note that the velocity scaling is size dependent, with the larger island close to linear and the smaller one sublinear.

increasing velocity increases the frequency of stick-slips, but basically not the average frictional force. However, perfect structurally superlubric sliding is expected to yield a linear dependence  $F_k \propto v$  on general grounds. As mentioned, the qualitative picture in this case is that the misfit dislocations that form the moiré pattern move during sliding as fast dissipative “Stokes quasiparticles,” thus exciting phonons in the medium and giving rise to smooth, viscous friction that is proportional to the velocity.

Viscous friction is actually more general than that and applies to pinned interfaces too, in two extreme limits. Physical reasoning and model studies show that stick-slip sliding, universal for pinned interfaces driven by sufficiently weak springs, survives in only a limited (even if large) velocity and temperature window. As sketched in Fig. 11(a), from Krylov and Frenken (2014), stick-slip sliding turns viscous when velocity is either high or low enough. At high velocity, typically when the kinetic energy exceeds the largest energy barrier energy  $(1/2)Mv^2 > U_0$ , barriers lose their grip, and friction turns “ballistic” (Guerra *et al.*, 2010), a regime where friction rises linearly with velocity. Conversely, at the low velocity limit and nonzero temperature, a nanoslider has ample time to thermally diffuse back and forth across barriers. In this condition Einstein’s viscous drift regime applies, a regime also referred to as thermolubric (Krylov and Frenken, 2014; Pellegrini *et al.*, 2019). In the vast velocity interval between these two limits (thermolubric and ballistic), friction is stick-slip-like, with logarithmic velocity dependence pervasively seen in 2D material sliding data, as in Fig. 11(b).

Temperature dependence will also differ in these three regimes. Medium and low speed stick-slip friction should gently drop upon increasing temperature by terms roughly like  $-\ln T$  (Sang, Dubé, and Grant, 2001; Dudko *et al.*, 2002; Krylov *et al.*, 2005) as thermal fluctuations help to overcome barriers. The negative temperature dependence shown in

Fig. 12(a) is compatible with the logarithmic velocity dependence of stick-slip sliding (Wang and Li, 2019; Liu *et al.*, 2020). Conversely, ultralow speed thermolubric and viscous friction drops much faster than logarithmic friction as the temperature rises. This is because in this regime the externally forced drift is a weak perturbation of thermal random walk, so the frictional damping  $\zeta$  obeys Einstein’s relation  $\zeta = k_B T/D$ . Here the linear  $T$  growth of  $\zeta$  is overcome by the much stronger Arrhenius-like exponential growth of diffusion coefficient  $D \propto \exp(-W/k_B T)$ , with  $W$  a typical barrier energy. However, high speed ballistic friction, which is also viscous with velocity, is predicted to grow linearly with temperature. In this regime, as exemplified by Guerra *et al.* (2010), phonon scattering of a fast slider is enhanced by the growing dynamic corrugation of the interface at higher temperature. After this preamble, we can look once again to the frictional simulation data of a prototypical 2D graphene interface.

In the OBC islands with a large twist angle and soft driving spring, stick-slip sliding is responsible for the weak velocity dependence [the red horizontal line in Fig. 11(c)] and the negatively correlated temperature dependence of friction [the red lower left curve in Fig. 12(b)]. The same slider pulled with a harder spring switches over to a linear velocity and temperature scaling frictional regime. In the latter case, we still expect a crossover to stick-slip at much lower velocities, but only for sufficiently large slider sizes. The situation changes for islands at small twist angle, where the moiré size becomes large, and the uncompensated moiré at the edges contributes additional sliding barrier. Thus, the roughly constant stick-slip friction at large twists [the red line in Fig. 11(c)] is replaced by the size-dependent velocity scaling: linear for the  $D_n = \sqrt{3}\lambda(n/2 + 1/8)$  cases ( $D_2 \approx 14$  nm) and sublinear for the others [Fig. 11(c)].

The limited but representative 2D material velocity-dependent results in experiments [shown in Fig. 11(b), left

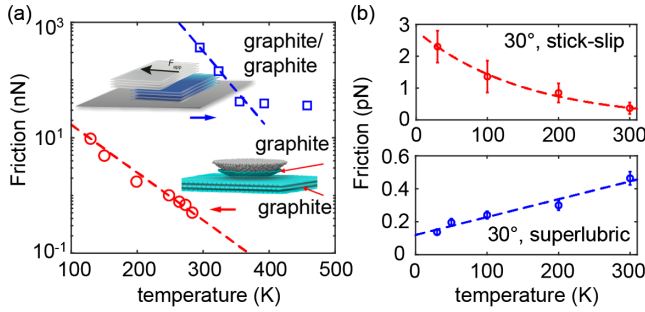


FIG. 12. Temperature dependence of graphene-graphene kinetic friction. (a) Experimental results. The red data (lower left) are for nanosized ultrahigh vacuum sliding (Liu *et al.*, 2020), while the blue data (upper right) pertain to microsized, ambient condition sliding (Wang and Li, 2019). The dashed lines are exponential fits reflecting an activated barrier crossing. The high-temperature saturation of microsized data may be an artifact due to the 5 nN sensitivity limit of the force sensor. (b) Simulated kinetic friction of a graphene island [Fig. 5(a)] with  $D = 2$  nm and  $\theta = 30^\circ$ . Red lines, stick-slip regime [ $K_p = 1$  N/m; Fig. 8(b)]; blue lines, superlubric regime [ $K_p = 100$  N/m; Fig. 8(b)] mimicking the structurally superlubric case. The red and blue dashed lines are exponential and linear fits, respectively.

shaded area] display a clear logarithmic velocity dependence. This confirms that stick-slip friction must be present at the nanoscale level (Buzio *et al.*, 2021, 2022), even when not visible in the overall friction traces. These systems (Song *et al.*, 2018; Wang and Li, 2019; Li, Li, Jiang, and Luo, 2020; Liu *et al.*, 2020), while not structurally superlubric, may still be structurally lubric, with their friction controlled by pinning from defects or edges, not from the slider's interior. For practitioners, nevertheless, these systems are often engineered as superlubric because of the small friction coefficient, as detailed in Sec. VII.

An interesting digression before closing the discussion of area and velocity dependence of friction in structurally lubric interfaces concerns the sliding of coaxial carbon nanotubes (CNTs) and of graphene nanoribbons (GNRs) on metal surfaces. In multiwalled CNTs of different chirality, friction is weakly dependent on length (Zhang *et al.*, 2013; Niguès *et al.*, 2014). This shows that the CNT friction originates from the edge: just two ends, while the interior is structurally superlubric and frictionless. This same observation applies to GNRs sliding on metal surfaces (Benassi *et al.*, 2015; Gigli *et al.*, 2017, 2018).

## VII. LOAD

### A. Ordinary and differential friction coefficients

The load dependence of sliding friction is historically represented by the friction coefficient  $\mu = F_f/F_N$ , where  $F_f$  and  $F_N$  are the friction force and normal load, respectively. The empirical proportionality between friction and load, dating back to Leonardo da Vinci and Amontons hundreds of years ago (Amontons, 1699; Dowson, 1979), makes the friction coefficient a widely used phenomenological parameter in macroscopic tribology. In the sliding of rough

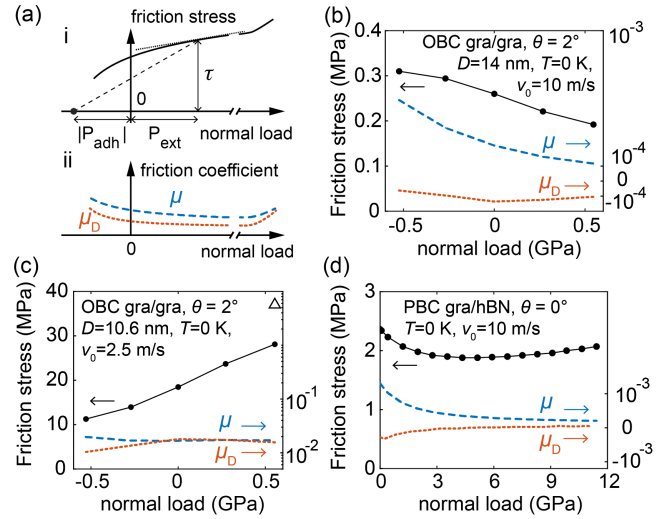


FIG. 13. Load dependence of 2D material sliding friction. (a) Schematic diagram contrasting the friction coefficient  $\mu$  and the differential friction coefficient  $\mu_D$ . The slopes of the dashed and dotted lines represent  $\mu$  and  $\mu_D$ , respectively. (b), (c) Simulated load dependence of kinetic friction in  $2^\circ$ -twisted islands of different sizes: (b)  $D = 14$  nm, representative of the superlubric regime, and (c)  $D = 10.6$  nm, representative of stick-slip regime; see Fig. 10(b). The inset triangle in the upper right corner shows a mere 30% increase in stick-slip friction force when  $v_0$  is increased 5000% under a 0.5 GPa load. (d) Simulated load dependence of large speed kinetic friction in infinite aligned graphene/h-BN heterostructures (an ideal structurally superlubric case). The blue dashed and red dotted lines represent  $\mu$  and  $\mu_D$ , respectively. Adapted from Mandelli *et al.*, 2019.

interfaces, the increase of friction with load is ordinarily attributed to the increase of contact points (the real contact area) and to the enhanced role of interface corrugation (Bowden and Tabor, 2001). In nanoscale friction, the variation with load is instead system dependent and generally not linear.

In 2D material interfaces with wide atomically smooth terraces in flat contact (Song *et al.*, 2018; Peng *et al.*, 2022), the load dependence of friction is also not linear. To begin with, friction is not zero even at zero external load. Physical adhesion effects due to van der Waals attractions and/or electrostatic interactions cancel out in rough interfaces, but they do not in 2D material interfaces, owing to their large terraces and limited roughness (Luan and Robbins, 2005; Erdemir and Martin, 2007). The result may be seen as an adhesion pressure  $P_{\text{adh}} \sim -A^{-1}dE_{\text{adh}}/dz|_{z=z_0}$ , where  $z_0$  is the nominal interlayer detachment distance. That is the distance where  $d^2E_{\text{adh}}/dz^2 = 0$  at which the friction force would vanish. At zero external load the kinetic frictional stress of real 2D material interfaces is generally nonzero, as sketched in Fig. 13(a), even at extremely low velocity. If the flat contact area is structurally lubric, then its interior contribution is negligible at such low velocities, and the zero-load friction is entirely due to stick-slip of the edges and defects. Figure 13(a) shows how the large adhesion in a 2D material interface influences the friction-load curve. The early onset of edge and defect friction at large negative load is the reason why friction remains nearly constant upon weakly increasing positive load.

TABLE I. Kinetic friction coefficient for structurally lubric homostructures from existing studies. The friction coefficient  $\mu$  at zero load estimated from Eq. (7), with  $P_{\text{ext}} = 0$  and  $|P_{\text{adh}}| \approx 1$  GPa. This quantity, not  $\mu_D$ , should be used to calculate dissipation.  $P_{\text{ext}}$  is the external normal load per unit area. HV, high vacuum.

Homostructures	Environment	$\mu$	$\mu_D$	$P_{\text{ext}}$	Reference
Graphene/graphene	MD, OBC	$4.8 \times 10^{-5}$	$-3.5 \times 10^{-4} - 5.6 \times 10^{-5}$	4 GPa	Wang, Wang, and Ma (2022)
Graphite/graphite	Ambient	$4.0 \times 10^{-6}$	$-4 \times 10^{-4} - 10^{-4}$	1.67 MPa	Vu <i>et al.</i> (2016)
Graphene/graphite	Ambient	$4.7 \times 10^{-3}$	$3 \times 10^{-3}$	$\sim 1$ GPa	Liu <i>et al.</i> (2017)
MoS <sub>2</sub> /MoS <sub>2</sub>	HV	$1.3 \times 10^{-4}$	...	...	Li <i>et al.</i> (2017)
Graphite/graphite	Ambient	$1.4 \times 10^{-5}$	$-3.3 \times 10^{-4} - 1.6 \times 10^{-4}$	7.78 MPa	Deng <i>et al.</i> (2018)
Graphite/graphite	UHV	$1.3 \times 10^{-4}$	$4 \times 10^{-5}$	$\sim 40$ MPa	Liu <i>et al.</i> (2020)
MoS <sub>2</sub> /MoS <sub>2</sub>	UHV	...	$2.5 \times 10^{-4}$	$\sim 25$ MPa	Liu <i>et al.</i> (2020)
Graphite/graphite	Ambient	$< 3.6 \times 10^{-6}$	...	28 MPa	Peng <i>et al.</i> (2020)

Conversely, above certain large loads, both static and kinetic friction may again increase (van Wijk *et al.*, 2013), reflecting the increased grip associated with distortions at the edge or defects.

The nonzero friction at zero load renders the naively defined friction coefficient  $\tilde{\mu} = \tau/P_{\text{ext}}$ , where  $\tau = F/A$  is the frictional shear stress and  $P_{\text{ext}} = F_N/A$  is the external normal pressure, divergent at zero load and therefore useless. To avoid this problem, practitioners often adopt the differential form  $\mu_D = d\tau/dP_{\text{ext}}$  (Gao *et al.*, 2004; Hod *et al.*, 2018). Yet, the differential friction coefficient  $\mu_D$  does not measure the energy dissipation, which is precisely what the friction coefficient was meant to do. A better definition of the friction coefficient  $\mu$  is obtained considering adhesion (Derjaguin, 1934) in the form

$$\mu = \frac{\tau}{P_{\text{ext}} + |P_{\text{adh}}|}, \quad (7)$$

where  $P_{\text{adh}}$  is the previously described adhesion pressure, a constant for each given 2D interface. The differential friction coefficient can be expressed as

$$\mu_D = \frac{\partial \tau}{\partial P_{\text{ext}}} = \mu + \frac{\partial \mu}{\partial P_{\text{ext}}}(P_{\text{ext}} + |P_{\text{adh}}|). \quad (8)$$

We illustrate the behavior of  $\mu$  and  $\mu_D$  versus load in the schematic of Fig. 13(a). For  $P_{\text{ext}} \rightarrow -|P_{\text{adh}}|$ , the detachment negative pressure, the effective total load vanishes, and  $\mu_D$  coincides with  $\mu$ . In this hypothetical limit, however, neither is well defined, for the numerator would vanish too. Moreover, nonuniform detachment would nucleate even before reaching the nominal detachment distance, and flatness of the interface would be lost. For all other loads  $P_{\text{ext}} > -|P_{\text{adh}}|$ ,  $\mu$ , geometrically corresponding to the slope of the dashed line in Fig. 13(a), makes good sense, and there are all reasons to use it.

First,  $\mu$  is generally larger than  $\mu_D$ . However, since  $|P_{\text{adh}}| \sim 1$  GPa is generally much larger than the experimental  $P_{\text{ext}}$ ,  $\mu_D$  and  $\mu$  should have similar orders of magnitude. The fact that  $\mu_D$  is straightforward to both measure and simulate justifies historically, if not physically, its adoption to qualify the load behavior of structurally lubric systems (Hod *et al.*, 2018). Currently, in fact, all 2D material interfaces with a small  $\mu_D$  are generically called superlubric. Experiments and simulations in 2D-material-based homointerfaces and

heterointerfaces (Tables I and II) report extremely low  $\mu_D$  values (Liu *et al.*, 2017, 2018; Deng *et al.*, 2018; Li, Gao, and Luo, 2018; Liu *et al.*, 2020) down to  $10^{-5}$  for structurally lubric twisted graphite-graphite contacts and graphite-MoS<sub>2</sub> contacts (Liu *et al.*, 2020), but generally do not provide  $\mu$ .

Second,  $\mu_D$  does not measure frictional dissipation (it is not even strictly positive), whereas  $\mu$ , which is strictly positive, does. A case in point where that issue strikes comes just when  $\mu_D < 0$ . A negative  $\mu_D$  [see Fig. 13(d)], generally due to load-induced “ironing” of corrugations, has been found in simulations, either of palladium-graphite systems (Sun *et al.*, 2018) or of systems with grain boundaries (Gao, Ouyang, Urbakh, and Hod, 2021) (with buckling corrugations), and twisted graphene-graphene contacts (with moiré corrugations). (Mandelli *et al.*, 2019; Wang, Wang, and Ma, 2022). Early experiments with graphite contacts (Vu *et al.*, 2016; Deng *et al.*, 2018) also probably involved negative  $\mu_D$  but did not make it emerge clearly, because the fitting of  $\mu_D$  had a large error. Despite its popularity, also mentioned in connection with the bearing capacity of structural superlubricity under load,<sup>2</sup> negative  $\mu_D$  has not yet been systematically confirmed in structurally lubric experiments.

Our own take on this theme is that the pursuit of a negative  $\mu_D$  is not in itself of real significance. It will at best signal efficient load-induced ironing of edge or defect corrugations and barriers and suggest nonmonotonicity of frictional stress and friction coefficient versus load, but not more than that. It may even be dangerous since the real friction coefficient can nonetheless be large (and unknown). Moreover, as we later show, load can in fact play the opposite effect, increasing the edge barrier rather than ironing it away, in which case  $\mu_D$  simply remains positive.

How large or small is the actual friction coefficient  $\mu$  for 2D structurally lubric interfaces? At present the answer is that we do not know. To obtain a simple order of magnitude, we insert in Eq. (7) an estimate of  $P_{\text{adh}}$ , as suggested from experiment (Li *et al.*, 2019) and theory (Ouyang *et al.*, 2018), of around

<sup>2</sup>A series of studies are pushing the upper limit of external load  $P_{\text{ext}}$  to the gigapascal range (Liu *et al.*, 2017; Li, Gao, and Luo, 2018; Xu, Sun *et al.*, 2022). There is, however, a practical upper limit to the bearing capacity. In graphite, at high normal loads (pressure on the order of 10 GPa) (Mao *et al.*, 2003; Martins *et al.*, 2017), bonds appear to begin forming between layers, causing the demise of structural lubricity.

TABLE II. Kinetic friction coefficient for structurally lubric heterostructures from existing studies.  $P_{\text{ext}}$  is the external normal load per unit area. The friction coefficient  $\mu$  at zero load was estimated from Eq. (7), with  $P_{\text{ext}} = 0$  and  $|P_{\text{adh}}| \approx 1$  GPa. This quantity, not  $\mu_D$ , should be used to calculate dissipation.  $P_{\text{ext}}$  is the external normal load per unit area.

Heterostructures	Environment	$\mu$	$\mu_D$	$P_{\text{ext}}$	Reference
Graphene/ <i>h</i> -BN	MD, PBC	$1.6 \times 10^{-4}$	$-2.5 \times 10^{-4} - 5 \times 10^{-5}$	12 GPa	Mandelli <i>et al.</i> (2019)
Graphene/ <i>h</i> -BN	Ambient	$2.7 \times 10^{-3}$	$2.5 \times 10^{-3}$	$\sim 1$ GPa	Liu <i>et al.</i> (2017)
Graphite/ <i>h</i> -BN	Ambient	$2.2 \times 10^{-5}$	$\leq 1.4 \times 10^{-4}$	11.1 MPa	Song <i>et al.</i> (2018)
Graphite/ <i>h</i> -BN	UHV	$1.2 \times 10^{-4}$	$4 \times 10^{-5}$	$\sim 40$ MPa	Liu <i>et al.</i> (2020)
Graphite/MoS <sub>2</sub>	UHV	$1.5 \times 10^{-4}$	$1.3 \times 10^{-4}$	$\sim 40$ MPa	Liu <i>et al.</i> (2020)
Au/graphite	Ambient	$1.2 \times 10^{-3}$	$1 \times 10^{-3}$	34.9 MPa	Li, Li, Chen <i>et al.</i> (2020)
MoS <sub>2</sub> /graphite	Dry N <sub>2</sub>	$2.6 \times 10^{-6}$	$\ll 10^{-3}$	$\sim 1$ MPa	Liao <i>et al.</i> (2022)
MoS <sub>2</sub> / <i>h</i> -BN	Dry N <sub>2</sub>	$2.3 \times 10^{-6}$	$\ll 10^{-3}$	$\sim 1$ MPa	Liao <i>et al.</i> (2022)

1 GPa in the case of graphene. This crude evaluation of  $\mu$  for various measured interfaces is given in Table I. The magnitude of  $\mu$  turns out to be generally of the order of  $10^{-4}$ , sometimes higher, and occasionally as low as  $10^{-6}$  for microscale graphite-graphite (Peng *et al.*, 2020) and MoS<sub>2</sub>-graphite contacts (Liao *et al.*, 2022). For comparison, the ice surface, the most familiar slippery surface in everyday life, has a friction coefficient of the order of  $10^{-2}$  (Kietzig, Hatzikiriakos, and Englezos, 2010), which is much larger. Summing up, to provide evidence of the low dissipative frictional character, it seems mandatory to go back to using  $\mu$  rather than  $\mu_D$  for the load dependence of friction in 2D material structural lubricity.

## B. Friction coefficient of 2D material interfaces

It is instructive at this point to illustrate the load dependence of 2D material friction by showing actual values from existing studies, in comparison with token simulation results. Tables I and II summarize some existing results, most of which are experimental. Table III shows graphene-graphene simulated friction coefficients, for large and small twist angles typified by 30° and 2°. We restrict to OBC island friction, while the PBC results are omitted as unrealistic because simulation velocities are many orders of magnitude too large when compared to standard nanofriction experiments, where  $v \sim 10^{-6}$  m/s or lower. The friction coefficient is estimated through Eq. (7) in all cases where it is missing from the original data.

In the experimental data the nature of kinetic friction can generally be argued to be stick-slip on account of the weak

logarithmic velocity dependence, while the interface twist angle is generally unknown. The simulation results offer the advantage of exploring a broader regime of parameters and the twist angle dependence.

On the whole, experimental and simulated friction coefficients appear to be comparable, even though as later explained that need not be significant. Experimental values confirm the well-known engineering superlubric, and structurally lubric, quality of 2D interfaces. Usefully, simulated results show the differing behavior of the friction and differential friction coefficients  $\mu$  and  $\mu_D$ . The first is positive and quite stable while the second is of variable sign, more volatile and less physically meaningful, although often of similar absolute magnitude, as expected because of the large value of  $|P_{\text{adh}}|$ . Where they differ,  $\mu$  is often not as low as  $\mu_D$  might have suggested. We stress again that, while  $\mu_D < 0$  merely indicates an effective pressure “ironing out” of edge and/or defect barriers, only  $\mu$  can gauge how important this effect is in terms of frictional energy dissipation.

*Large twist angles.* Regarding  $\theta = 30^\circ$  in Table III, several features stand out. The first is that the static friction coefficient is much larger than the kinetic friction. The second is that the absolute value of the kinetic friction coefficient  $\mu$  is extremely low, of the order of  $10^{-5}$ . Both features are compatible with a structurally lubric friction. However, friction is not completely structurally superlubric, owing to the nonzero static friction coefficient (of the order of  $10^{-3}$  in that case). The third point is that the differential friction coefficient is negative. The negative sign indicates that the barrier-generating defects (here the island edges) are being effectively ironed out by

TABLE III. Friction coefficient from graphene-graphene interface simulations. The value of the friction coefficient  $\mu$ , according to Eq. (7), is obtained with  $|P_{\text{adh}}| = 1.1$  GPa (Li *et al.*, 2019). The twist angle dependence of  $P_{\text{adh}}$  is negligible (Wang *et al.*, 2015).

Twist angle (deg)	2		30	
$P_{\text{ext}}$ (GPa)	−0.5–0.5		0–1.0	
Fraction type	Kinetic (stick-slip)	Kinetic (smooth)	Kinetic (smooth)	Static
Temperature (K)	0		300	0
Diameter (nm)	10.6	14	8	
Velocity (m/s)	2.5	10	10	
$\mu$ at zero $P_{\text{ext}}$	$1.68 \times 10^{-2}$	$2.36 \times 10^{-4}$	$5.8 \times 10^{-5}$	$2.9 \times 10^{-3}$
$\mu$ at max $P_{\text{ext}}$	$1.70 \times 10^{-2}$	$1.17 \times 10^{-4}$	$2.5 \times 10^{-5}$	$2.0 \times 10^{-3}$
$\mu_D$ at zero $P_{\text{ext}}$	$1.79 \times 10^{-2}$	$-1.36 \times 10^{-4}$	$-5.8 \times 10^{-5}$	$5.0 \times 10^{-4}$
$\mu_D$ at max $P_{\text{ext}}$	$1.57 \times 10^{-2}$	$-1.04 \times 10^{-4}$	$-1.8 \times 10^{-5}$	$2.2 \times 10^{-4}$



the load. The ironing effect, effective here for kinetic friction, is seen in this case to affect the static friction much less.

While the previous observations are instructive about friction of strongly incommensurate interfaces epitomized by graphene-graphene interactions at large twist angle, the quantitative comparison with experimental friction coefficients of Tables I and II demands critical attention. On the whole, in fact, large twist angle theoretical friction coefficients show similar orders of magnitude as experiments, but that in itself is not significant. The reason is that, as discussed earlier, smooth sliding implies proportionality of the shear stress  $F/A$  to  $v_0$ , while edge-dominated friction stress demands proportionality to  $A^{\alpha-1}$  with  $\alpha < 1/2$ . Extrapolation from the simulation velocity of 10 m/s to realistically small velocities and from the small island area of just 8 nm diameter to realistically larger areas leads to theoretical friction coefficients many orders of magnitude below the experimental ones. This disagreement indicates in our view that in most experiments there must be large defect-related barriers, possibly acting at different spatial points, that give rise to local stick-slip sliding, thus canceling smooth sliding. A careful study of experimental velocity, twist angle, and area dependence is needed to clear that crucial point.

*Small twist angles.* The friction coefficient is complex in the small twist  $S$  regime where, as shown in Fig. 10(b), the frictional behavior of small islands oscillates between high friction stick-slip maxima and low superlubriclike minima. Table III exemplifies some of that complexity by comparing the kinetic friction coefficients at velocities between 2.5 and 10 m/s of  $\theta = 2^\circ$  islands with two representative small diameters  $D = 10.6$  nm (maximum friction, stick-slip) and 14 nm (minimum friction, smooth sliding) that are chosen as the first members of their families; see Fig. 10(b) (simulated at  $T = 0$  for additional clarity). The radius  $D = 10.6$  nm and all larger members of its family exhibit a large  $\mu$  and a positive  $\mu_D$  owing to strong stick-slip friction, caused by the edge, that creates a barrier against entry and exit of uncompensated moiré portions. This is also illustrated in Fig. 7 (Koren and Duerig, 2016a). Conversely, Table III and Figs. 13(b) and 13(c) show much smaller  $\mu$  and a negative  $\mu_D$  in the 14 nm diameter where, as shown by Fig. 11(c), there is only a weak edge effect, and friction at this large speed is viscous. This is because no uncompensated moirés are attempting to cross the edge.

Remember that these results strongly depend on the island area and velocity. Based on Fig. 10(b), we anticipate that at sufficiently large island sizes [Eq. (11)] stick-slip behavior with larger  $\mu$  and positive  $\mu_D$  becomes universal. In that limit, the weak friction family will merge with the strong ones. Moreover, we expect the merging to also occur at constant island area at low enough velocity. That happens with a crossover from viscous to stick-slip behavior similar to that of Fig. 11(b). This simplified understanding is based on the circular shape of the island. In real systems, polygonal tracts of the edge are more likely to take over. This will make the picture more complicated and generic size dependence, therefore, unpredictable.

To become more specific before closing the load dependence, we compare the stick-slip friction coefficients of the

small twist angle simulated graphene interface in Table III to the data of Tables I and II. These stick-slip friction coefficients are not dependent on velocity and elicit complementary comments to the large twist case. First, the theoretical values of Table III are orders of magnitude larger than the experimental ones. The island sizes are small, but since friction grows sublinearly with area the friction coefficient will decrease at large areas down to values closer to the experimental range. Second, stick-slip of Table III has a positive differential friction coefficient, showing that, unlike suggestions of PBC simulations (which might in this respect be considered academic), load appears to increase the energy barrier felt by the moiré rather than ironing it away, an observation that may explain why negative  $\mu_D$  is so difficult to find in experiments.

## VIII. ELASTICITY

Theoretical work has long discussed the structural and tribological effect of elasticity (Hurtado and Kim, 1999; Persson and Tosatti, 1999; Müser, 2004; Benassi *et al.*, 2015; Ma, Benassi *et al.*, 2015; Mandelli *et al.*, 2018; Feng and Xu, 2022). Elastic effects are dependent upon system dimensionality (Müser, 2004) and size: important at large slider diameters and irrelevant for small ones, where the slider is closer to a rigid flake. In this section we discuss what mechanism determines a typical crossover diameter  $D$  separating the two regimes, and in what way this might depend on the specific properties of a 2D material interface. Different mechanisms suggest different critical lengths.

For macroscopic interfaces, which are generally rough and multicontact, a well-known critical size is the elastic coherence length, or Larkin length,  $D_L$  (Larkin and Ovchinnikov, 1979) dividing the regimes where different contact points act collectively or separately. Its theoretical estimate is  $D_L/D \sim \exp(Yd/\sigma_y D)^2$ , where  $D$  is the diameter of the contact,  $Y$  is Young's modulus,  $d$  is the average distance between random contacts, and  $\sigma_y$  is the yield stress (Persson and Tosatti, 1999; Vanossi *et al.*, 2013). Originally devised for flux lattice creep and important all the way up to earthquakes, this rough interface scenario is generally far from relevant in real 2D material nanoscale and mesoscale interfaces, and we do not concern ourselves further with it.

In mesoscopic, relatively defect-free crystalline contacts, which is the case for pristine 2D material interfaces, the relevant crossover size is the elastic length  $D_e$ . Generally invoked to describe the competition between intraslider shear modulus  $G$  and the slider-substrate interaction, in turn controlling the shear strength  $\tau_{\max}$  (Müser, 2004; Sharp, Pastewka, and Robbins, 2016), the elastic length is given as

$$D_e/a \sim G/\tau_{\max}. \quad (9)$$

Once the slider diameter  $D$  exceeds  $D_e$ , whose magnitude varies for different systems and driving methods (Benassi *et al.*, 2015; Mandelli *et al.*, 2018), a dislocation nucleates at the edge, as exemplified in Figs. 14(a) and 14(b), thus enhancing the static friction (Hurtado and Kim, 1999; Varini *et al.*, 2015; Sharp, Pastewka, and Robbins, 2016).

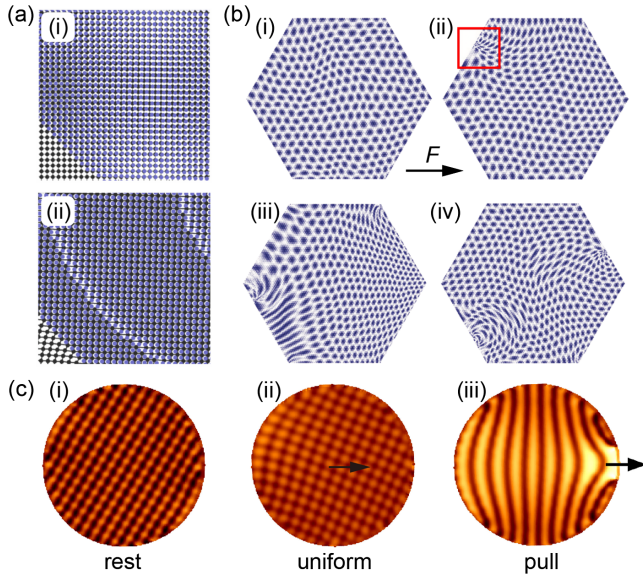


FIG. 14. (a) Elastic deformation of the flexible substrate (black lattice underneath) in incommensurate contact with a rigid circular slider (upper blue layer). (i) Stiff substrate ( $G/\tau_{\max} = 256$ ). (ii) Soft substrate ( $G/\tau_{\max} = 1$ ). Adapted from Sharp, Pastewka, and Robbins, 2016. (b) Moiré evolution of the simulated incommensurate Kr/Pb(111) contacts. Colors range from blue (dark) when Kr atoms are maximally coincident with Pb atoms to white (bright) when they are minimally coincident. (i) Stationary system (dragging force  $F = 0$ ). (ii) System with  $F = 2.24$  nN (just above the maximum static friction). The soliton entering from the left edge is highlighted by the red square. (iii) System after sliding of the island center by 1.0 surface lattice spacing. (iv) System when the sliding is 1.5 lattice spacings and a soliton exits the island on the right-hand side. Adapted from Varini *et al.*, 2015. (c) Strain distribution of (ii) a uniformly driven vs (iii) an edge-pulled 2D harmonic lattice island submitted to a slightly less dense, and therefore incommensurate, 2D sinusoidal potential (“Frenkel-Kontorova”-type model) compared to its static state (i). Colors range from white (bright) for perfect local coincidence to black (dark) for maximal local mismatch. The edge-pulling procedure favors the formation of locally strained commensurate regions, thereby enhancing the static friction, and the ensuing stick-slip in comparison to the uniformly driven system (Mandelli *et al.*, 2018; Vanossi, Bechinger, and Urbakh, 2020). Note also the corresponding moiré switch from 2D to striped.

In structurally lubric graphene interfaces where  $G \approx 300$  GPa (Liu, Metcalf *et al.*, 2012) and  $\tau_{\max} \approx 100$  MPa (Wang *et al.*, 2022), one would estimate  $D_e \approx 1$   $\mu\text{m}$ . Even after the dislocation has nucleated, sublinear static friction controlled by edges must generally persist (Varini *et al.*, 2015) up to some larger size  $D_t$  where a train of dislocations enters the slider’s interior. For  $D > D_t$  the static friction will eventually grow proportionally to area (Hurtado and Kim, 1999; Sharp, Pastewka, and Robbins, 2016).

For stiff sliders, as 2D materials are, the sublinear size scaling of static friction is in fact known to persist for much larger diameters  $D \gg D_e$  (Sharp, Pastewka, and Robbins, 2016). Model estimates of the  $D_t$  where structural lubricity fails in 2D material stacks (Ma, Benassi *et al.*, 2015) are far

larger than even the size of the experiments. Among examples, graphite mesas of micrometer-size (Qu *et al.*, 2020) and 1D carbon nanotubes of centimeter length (Zhang *et al.*, 2013) support a much wider range of structural lubricity than ordinary 3D crystalline interfaces.

In addition to static friction, elasticity influences kinetic friction of 2D materials interfaces, deciding, in particular, whether it will be smooth sliding or stick-slip sliding. Two extra factors matter for kinetic friction: (i) large static friction favors stick-slip sliding but does not actually determine it, and (ii) the effective lateral stiffness  $K_p$  becomes highly important. With layer elasticity in mind, we therefore look for an upper size  $D_c$  above which it will cause stick-slip sliding, even without destroying structural lubricity. A useful route is suggested by the PT model. Consider a 2D material island whose sliding must negotiate an energy barrier caused by the edge. Contact elasticity and spring stiffness together determine whether the sliding can be smooth despite the barrier or whether a mechanical instability will take place and give rise, for sufficiently low velocities, to stick-slip (Vanossi *et al.*, 2013). If the effective lateral stiffness  $K_p$  is soft enough, resulting in  $\eta = 2\pi^2 U_0 / K_p a^2 \gg 1$ , stick-slip sliding will necessarily ensue for all slider diameters. This regime may indeed be close to actual experiments, where the underlying stick-slip regime is proven by the ubiquitous logarithmic velocity dependence. However, if  $K_p$  is hard enough, the sliding can still be either smooth or stick-slip depending whether the diameter of the slider is smaller or larger than a maximal critical  $D_c^{\max}$ .

Determined by three factors, the barrier  $U_0$ , the pulling spring stiffness  $K_p$ , and the intrainland stiffness  $k_{\text{isl}}$ , a more general  $D_c$  is estimated by requiring that the joint spring-island inverse stiffness  $K_{\text{eff}}^{-1} = k_{\text{isl}}^{-1}(D) + K_p^{-1}$  satisfy the PT-like inequality  $\eta \geq 1$  [Eq. (5)]. An upper bound for the critical circular slider diameter  $D_c$  is obtained in the limit  $K_p^{-1} = 0$  where stick-slip sliding occurs if the effective island in-plane stiffness  $k_{\text{isl}}$  alone satisfies the inequality  $k_{\text{isl}}(D) < 2\pi^2 U_0(D) / a^2$ , where  $a$  is the lattice spacing of the substrate. For an edge-pinned circular flake with uniformly distributed in-plane dragging force along  $x$ , we obtain through fitting simulations of a circular island with a pinned circumference a displacement field that is extremely well represented by the form

$$u_x(x, y) = \delta_x \left[ 1 - \frac{4(x^2 + y^2)}{D^2} \right], \quad u_y(x, y) = 0, \quad (10)$$

with the corresponding strain field under the assumption of small deformation:  $\epsilon_{xx}(x, y) = -8\delta_x x / D^2$  and  $\epsilon_{xy}(x, y) = -4\delta_x y / D^2$ . By equating strain energy  $(1/2)k_{\text{isl}}\delta_x^2 = (1/2)\iint_A (Y_{2D}\epsilon_{xx}^2 + 2G_{2D}\epsilon_{xy}^2) dx dy$ , we get  $k_{\text{isl}} \sim \pi Y_{2D}$ , where  $Y_{2D}$  and  $G_{2D}$  are the 2D Young’s modulus and shear modulus and  $A = \pi D^2 / 4$  is the contact area of the flake. We see that the effective stiffness  $k_{\text{isl}}$  of a circular 2D island is independent of the diameter. However, owing to the emergence of the relevant localized elastic distortions, this property will not hold if the slider is pulled or pushed inhomogeneously, for example, by one side. This situation, in which stick-slip friction is strongly

enhanced, is illustrated in Fig. 14(c) and detailed in the caption (Vanossi, Bechinger, and Urbakh, 2020).

What does depend on diameter in all cases is the effective barrier  $U_0$  that pins the circular island, growing as  $U_0 \sim U_a(D/a)^{1/2}$ . Hence,  $D_c^{\max}/a = (Y_{2D}a^2/2\pi U_a)^2$  (obtained for  $K_p = \infty$ ) is the slider's diameter upper bound above which smooth sliding is impossible, and mechanical instability will arise for low velocity and low temperatures. In the general case, we thus obtain

$$D_c/a = \left[ \frac{a^2 Y_{2D}}{2\pi U_a (1 + \pi K_p^{-1} Y_{2D})} \right]^2, \quad (11)$$

which is a clean new result resulting from Eq. (5) for a uniformly pulled circular slider of 2D material.

This predicted critical diameter  $D_c$  for mechanical instability and consequent stick-slip friction will get arbitrarily small for a sufficiently soft external spring  $K_p$ . But how large will it get in practice for a hypothetically super hard spring  $K_p \rightarrow \infty$ ? Approximating  $Y_{2D}a^2 \sim Ga^3$  and  $U_a \sim \tau_{\max}a^3$ , one can rewrite Eq. (11) for  $K_p = \infty$  as  $D_c^{\max}/a \sim (G/\tau_{\max})^2$ . Compared to  $D_e/a \sim G/\tau_{\max}$ , one sees that in this limit  $D_c > D_e$  for structurally lubric 2D materials where  $G/\tau_{\max} \gg 1$ . Therefore, if a 2D slider can be pulled with a hard effectively spring  $K_p$  and if the edge energy barrier  $U_a$  is large enough, there is a range of diameters between  $D_c$  and  $D_e$  where the sliding remains smooth. To illustrate the opposite behavior, for the 30° twisted graphene interface of Fig. 10(a), the barrier  $U_a$  is only about 17 meV. With  $Y_{2D} = 300$  N/m (Memarian, Fereidoon, and Darvish Ganji, 2015), the maximal critical size  $D_c^{\max}$  is as large as 280  $\mu\text{m}$ , which exceeds  $D_e \approx 1$   $\mu\text{m}$ . The  $D_c$  with finite  $K_p$  (estimated from experiments to be  $\sim 30$  N/m) is 260 nm, several orders of magnitude smaller.

More generally, besides a soft pulling device, the critical size  $D_c$  for stick-slip onset also depends on other variables, including particularly shape, mutual lattice orientation, and shearing direction (Wang, Cao *et al.*, 2019). In graphene interfaces the critical  $D_c$  decreases for decreasing twist angles from regime  $L$  to regimes  $I$  and  $S$ , where the barrier  $U_a$  is larger, resulting in the larger friction shown in Figs. 10(a) and 10(b).

Summing up, for 2D materials where  $G/\tau_{\max}$  is large, the elastic length  $D_e$  of Eq. (9) identifies the size where elasticity permits nucleation of an edge dislocation, raising static friction. Independently,  $D_c$  of Eq. (11) is the elasticity-induced threshold of stick-slip friction. Structural lubricity persists in both cases. The threshold size  $D_c$  can also be increased by, for example, lifting the island edges (Huang, *et al.*, 2023). There must, however, be an even larger size  $D_t$  where dislocations finally uniformly invade the slider above which the friction turns proportional to area, marking the failure of structural lubricity.

## IX. DEFECTS

Thus far we have reviewed and discussed the size, velocity, temperature, and load dependence of friction together with the effects from elasticity for structurally lubric 2D material interfaces. NEMD simulations helped us understand and

rationalize physical phenomena and frictional data. Defect-free PBC simulations, in particular, are important for getting the idealized physical picture. When PBC simulations were compared to finite island OBC ones, it was invariably noted that many key differences were made by defects, in our case exemplified by edges that mark the boundary of the islands.

In practice, real 2D material interfaces are more complex than that. Physical and chemical complications arising from defects include, besides shapes of sliders (Luo *et al.*, 2011; Dietzel *et al.*, 2013; Özoğul *et al.*, 2017), edge chemisorption (Gongyang *et al.*, 2020), corrugation by contaminants at the interfaces, other imperfections such as grain boundaries (Červenka and Flipse, 2009; Yazyev and Louie, 2010; Yazyev and Chen, 2014), vacancies (Hashimoto *et al.*, 2004; Gajurel *et al.*, 2017), etc., all playing an important role. Each type of defect introduces its own specific energy barriers against sliding, influencing in turn the frictional behavior of real 2D material interfaces, even when they are nominally structurally lubric. While a review of these defects is beyond our scope here, we mention some of the most important ones before closing this Colloquium.

### A. Shape of sliders

As mentioned in Sec. VIII, circular islands and flakes discussed in our modeling are heavily idealized. Despite a few circular-shape-based experiments (Koren *et al.*, 2015; Li *et al.*, 2017; Ribeiro-Palau *et al.*, 2018; Finney *et al.*, 2019), most data refer to different shapes. In particular, straight-edged polygon shapes are common (with the straight edges reflecting the robust 2D crystalline structure of the island or flake), as sketched in Fig. 15(a). Several theoretical studies discussed this point (de Wijn, 2012; Varini *et al.*, 2015; Koren and Duerig, 2016a; Dietzel *et al.*, 2018; Wang, Cao *et al.*, 2019; Yan *et al.*, 2024) and found differently sized scalings of static friction for different shapes, with the exponent ranging from 0 to 1/2. This variability reflected the differing mismatch of the edge orientation with the substrate lattice. Although the

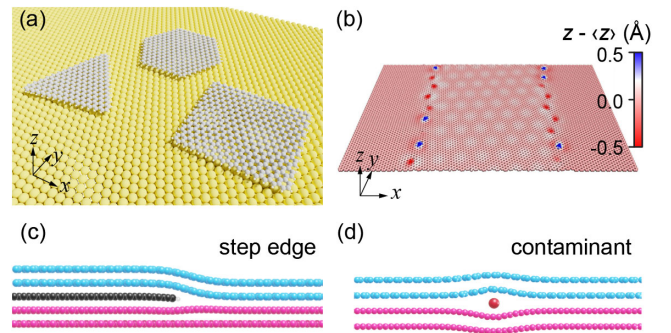


FIG. 15. Sketch of various defects. (a) Slider with different shapes, i.e., a different number of edges and corners. (b) Grain boundaries at the graphene interface. Color represents the out-of-plane displacement. From Gao, Ouyang, Urbakh, and Hod, 2021. (c) Step edge exposed to the sliding interface. Viewed from top to bottom, blue, black, and pink are the slider, the step edge, and the substrate, respectively. (d) Particle-contaminated graphene interface. Viewed from top to bottom, blue, red, and pink are the slider, the contaminated particle, and the substrate, respectively.

kinetic friction size scaling should eventually tend to linear when the contact area  $A \rightarrow \infty$ , the limit where the sublinear contribution from the edge can be neglected is difficult to reach in practice. Generally, owing also to the relatively high dissipation at edges (Varini *et al.*, 2015; Liao *et al.*, 2022), the size- and shape-dependent sublinear scaling behavior prevails. An especially large shape contribution to friction may be expected from sharp corners and protrusions; locations that enhance adhesion may transform into “pivots,” causing islands to rotate. We expect future theoretical and experimental studies to verify these expectations and provide further understanding.

## B. Grain boundaries

In the real 2D materials samples where macroscale engineering superlubricity is being sought and studied, extended lattice defects such as grain boundaries are inevitable (Tison *et al.*, 2014; Yazyev and Chen, 2014), and understanding their effect on friction is important. An effort was attempted in a series of carefully designed MD simulations (Gao, Ouyang, Hod, and Urbakh, 2021; Gao, Ouyang, Urbakh, and Hod, 2021; Gao, Urbakh, and Hod, 2022). Shear-induced buckling and unbuckling of the grain boundary is shown to affect the kinetic friction [Fig. 15(b)], resulting in a nonmonotonic dependence of friction upon load and temperature. Nevertheless, from the perspective of engineering superlubricity, the differential friction coefficient of the grain-boundary-containing systems is still below  $10^{-3}$  for a linear concentration of grain boundaries of  $0.0838 \text{ nm}^{-1}$ .

## C. Step edges

Experiments and simulations find that the ultralow friction of structural lubricity can be destroyed by the presence of steps [Fig. 15(c)] within the sliding interface (Wang *et al.*, 2020). Simulations further suggest that a large part of the extra friction is due to the violent, large out-of-plane displacement of the step-free slider as it surmounts the step edge of the substrate (Chen *et al.*, 2019; Wang *et al.*, 2020). The pinning caused by the step can change friction from smooth to stick-slip motion, destroying the main feature of structural lubricity. Buried steps, on the other hand (Wang *et al.*, 2020), and their milder corrugation propagated at the sliding interface (Peng *et al.*, 2022) have not been reported to cause effects of comparable significance. A remaining question is: At what depth should a step lie for the influence on friction to become irrelevant?

## D. Contaminants

It is generally accepted that structural lubricity requires the interface to be perfectly regular and, in particular, ultraclean. In common frictional setups, however, adsorbed gases and contaminants are rife, including measurements in fully ambient conditions (He, Müser, and Robbins, 1999; Li *et al.*, 2013, 2015). The presence of contaminants should intuitively lead to an increase in friction (Ouyang, de Wijn, and Urbakh, 2018), including the loss of superlubricity (Müser, Wenning, and Robbins, 2001), an expectation confirmed by recent

experiments and simulations (Deng *et al.*, 2018; Cheng and Ma, 2020; Wang *et al.*, 2022). In our prototypical simulation with  $30^\circ$ -twisted graphite system ( $T = 300 \text{ K}$  and  $v_0 = 30 \text{ m/s}$ ), the friction stress increases from  $\sim 10 \text{ kPa}$  to  $352 \pm 56 \text{ kPa}$  when one contaminate particle with number density  $0.0244 \text{ nm}^{-2}$  is introduced [Fig. 15(d)]. The presence of the contaminants results in stick-slip motion with a sublinear velocity scaling: when the velocity is reduced to  $10 \text{ m/s}$ , the friction stress becomes  $345 \pm 39 \text{ kPa}$ , which is almost unchanged. However, tribological running in, showing a friction decrease during repeated sliding of graphite contacts, was observed (Deng *et al.*, 2018) and explained by self-cleaning (Liu *et al.*, 2011; Ma, Sokolov *et al.*, 2015). Contaminants may also be removed by temperature, thereby artificially causing lower friction at higher temperatures (Wang and Li, 2019). However, contaminants such as water molecules (Falk *et al.*, 2010) and graphitic nanoflakes (Li, Gao, and Luo, 2018) serve as lubricants, thereby yielding lower friction.

A recent experiment conducted by intentionally introducing airborne contaminants into microscale superlubric graphite contacts showed that, although the friction stress increases (from  $10 \text{ kPa}$  to  $50 \text{ kPa}$ ) as the concentration of contaminants increases, the key features of engineering superlubricity, i.e., the ultralow friction and differential friction coefficient, are well preserved (Wang *et al.*, 2022). In the case of graphite/*h*-BN heterostructures, data in ambient conditions (where contaminants are expected) indicated that the friction force exhibits a  $60^\circ$  rotational symmetry with both the twist angle (Song *et al.*, 2018) and the sliding angle (Song *et al.*, 2021), suggesting that the interface retains its bulklike structure and symmetry. The sliding of gold nanoparticles on HOPG have been studied in both UHV (Dietzel *et al.*, 2013) and ambient conditions (Cihan *et al.*, 2016), yielding friction stresses of the same magnitude and similar scaling effects [Figs. 10(d) and 10(f)]. These experiments imply the robustness of structural lubricity, possibly implying low contamination, or else the low impact of contaminants, which could even be swept out when the slider-substrate adhesion is strong. One should expect future experiments and simulations to provide a clearer understanding of these phenomena following well designed surface science protocols, starting with clean interfaces and then introducing single well-defined contaminants.

## X. SUMMARY

We conclude the Colloquium by recalling the main outcomes and conclusions about friction of 2D structurally lubric interfaces. Our understanding, based on existing studies and illustrated by simulations of a specific graphene-graphene example, is proposed as relevant to the broader variety of 2D material sliding interfaces.

*Area dependence.* Structurally superlubric sliding causes a linear growth of kinetic friction with area (due to swift moiré flight) along with zero static friction. In the experimentally more relevant case of structural lubricity, the area dependence of static friction is generally sublinear. This also holds for kinetic friction, for soft effective stiffness where  $\eta > 1$  [Eq. (5)], and when the contact size is below the critical size  $D_c$ . Above the critical size  $D_c$ , both static and kinetic friction are proportional to area. For defect-ridden 2D material

interfaces that are merely engineering superlubric, the frictional behavior depends on the nature and distribution of the pinning agents. A uniform distribution will naturally cause static and kinetic friction to grow proportionally to area. The moiré pattern and its size and evolution are also crucial in 2D material friction. For example, at small twist angles (*S* regime) and for a circular slider shape, the kinetic friction is predicted to oscillate with increasing size. This reflects the energy barriers caused by the uncompensated moirés at the edges as the moiré nodes cross the slider's perimeter. These oscillations with size, even if difficult to address experimentally, are both predicted and observed in colloidal flakes (Cao *et al.*, 2022) and deserve specific research for 2D materials.

*Velocity and temperature dependence.* The linear velocity dependence of kinetic friction is a hallmark of structural superlubricity. With negligible static friction and weak moiré dissipation, structurally superlubric friction falls far below measurable magnitudes. Measurable values would require a sliding velocity of 1 m/s or higher, which is many orders of magnitude above current experiments, even if it is common in simulations. In experimental structurally lubric sliders whose static friction is nonzero, the velocity dependence is not linear but logarithmic. This always implies stick-slip friction, even when interference among pinning spots might have canceled its straight sawtoothlike evidence in force traces, an expected cancellation for large sliders (Braun *et al.*, 2012). Crossovers from logarithmic to linear regimes are always possible. Stick-slip sliding can be stopped in favor of thermolubric sliding (Krylov and Frenken, 2014) at the lowest speeds and/or highest temperatures, and of ballistic sliding (Guerra *et al.*, 2010) at the highest speeds. Both regimes imply linear velocity dependence, even if neither is experimentally common in 2D material friction. In some simulation studies, the high speed ballistic behavior is sometimes mistaken for structural superlubricity.

*Load dependence.* In genuine structural superlubricity the static friction is zero, regardless of load. Unlike, for example, colloid monolayers (Brazda *et al.*, 2018), we note that so far there has been no evidence that a load increase could induce an Aubry-type pinning transition in 2D material sliding. Simulations (high velocity) suggest that load may iron out the moiré corrugation, thereby reducing structurally superlubric friction (Mandelli *et al.*, 2019). The load dependence of experimentally relevant structural or engineering lubric friction, however, depends on the diverse effects that load can have on the edges and other pinning defects. The effective load determining the true, absolute friction coefficient must include a large adhesive pressure, as large as 1 GPa in graphene-type interfaces. This makes the physically significant friction coefficient of 2D material interfaces small, but not as small as the commonly used differential friction coefficient. Use of the latter is dubious because it does not measure frictional dissipation. It thus seems advisable to resume the use of an ordinary friction coefficient that is properly defined following Derjaguin (1934).

*Elasticity.* The effect of elasticity in large 2D sliding islands demands a fresh approach, owing to the extreme in-plane stiffness of these systems. For a circular shape with edge pinning, one can identify a novel critical diameter [Eq. (11)]

above which structurally lubric sliding will develop a mechanical instability and necessarily enter the stick-slip regime.

*Defects.* Finally and not surprisingly, realistic defects introduce havoc into this picture with each type opening a special chapter deserving its own special attention. The special role of the omnipresent slider's edge has been especially emphasized.

*Terminology.* It is suggested to avoid confusing terms sometimes found in the literature by introducing a distinction between three types of frictional behavior. Structural superlubricity is reserved for the essentially academic case of zero static friction. Although only accessible in simulations thus far, understanding this regime is important in the physics of 2D material interfaces (Wang, Ma, and Tosatti, 2023). Structural lubricity designates cases where the interface is incommensurate with a defect-free interior, but where static friction is nonzero owing to pinning by, for example, the slider's edge. We then propose that cases where the friction coefficient is small (typically lower than  $10^{-2}$ ) be called engineering superlubric. In this connection, further semantic confusion should be avoided between ordinary and differential friction coefficients. For some reason, this confusion is a dangerous current habit.

Many key points still remain to be addressed. Multiscale experiments and simulations are required to verify the large-scale friction scaling, which presently is mostly extrapolated. Experiments, for example, those examining frictional noise, could and should be designed to directly pinpoint the elusive but unquestionable underlying stick-slip friction of engineering superlubric systems. Experiments could explore the crossover from stick-slip to superlubric friction that a sliding island may undergo when the driver changes from soft to stiff, provided that the shape and size permit smooth sliding, such as in Fig. 8(b). This would enable access to superlubriclike kinetic friction in a real-world finite-size system. The sliding behaviors for small twist systems, where the interfacial structure is different than that of large twists, are also interesting and lack existing studies. It will also be desirable to extend the experimental velocity ranges to locate the crossover from stick-slip to the high velocity ballistic regime. Attacking these and related problems not only will solidify theoretical bases of superlubricity but will also offer keys to its practical application. Many other points, more speculative but involving real or potential questions, promising applications, and corresponding urgent problems, deserve mention. Among them are the following:

- Friction of freestanding or quasifreestanding 2D materials interfaces (Riedl *et al.*, 2009; Butz *et al.*, 2014). Despite the strong restriction from the substrate, the out-of-plane deformation of adsorbed 2D materials dominates the friction of structurally lubric systems. For freestanding systems, new phenomena brought about by out-of-plane flexural deformability are worth exploring (Wang *et al.*, 2023).
- Variety of 2D materials with structurally lubric behavior. Is graphene the ideal material for structural lubricity? Are there many more natural or engineered functional materials with better properties, such as larger intralayer-to-interlayer interaction ratios? Experiments as well as first-principles simulations can help reveal these properties for various contacts (Levita *et al.*, 2015; Losi,

Restuccia, and Righi, 2020; Gao, Wu *et al.*, 2021; Xu, Yu *et al.*, 2022). In addition, the development of machine learning approaches (Rowe *et al.*, 2018; Baboukani *et al.*, 2020) may further encourage research on this and related topics.

- Electronic friction in twisted bilayers, friction under external field (thermal, electric, magnetic, etc.) (J. Wang *et al.*, 2016; Belviso *et al.*, 2020; Song *et al.*, 2022).
- Rotational friction is also interesting but has been less explored (Koren *et al.*, 2015; Ribeiro-Palau *et al.*, 2018; Finney *et al.*, 2019; Yang and Zhang, 2021; Cao *et al.*, 2022).
- Potential applications: Structural lubricity is promising in the application of nanoelectromechanical and microelectromechanical systems, including nanogenerators, nano-oscillators, nanotips of hard drives, and nanorobotics (Zheng and Jiang, 2002; Huang, Lin, and Zheng, 2020; Huang *et al.*, 2021; Wu *et al.*, 2021). The dry interfaces with ultralow friction and high current stability (Lang *et al.*, 2021) can play important roles in precision instruments such as aerospace slip rings. Beyond these, the large number of combinations of homointerfaces and heterointerfaces composed of diverse 2D materials give the interface various physical properties, and thus wider applications.

We close hoping to have shed some light on and encouraged discussion of the questions that animate the pinning and sliding of 2D superlubric material interfaces. Answering these questions is important for understanding their physics, as well as for the development of current and future technologies.

## ACKNOWLEDGMENTS

We express our gratitude to X. Gao, M. Kisiel, N. Manini, E. Meyer, R. Pawlak, A. Silva, and M. Urbakh for the collaboration and helpful discussions. This work was carried out under ERC ULTRADISS Contract No. 834402. Support from the Italian Ministry of University and Research through PRIN UTFROM Grant No. 20178PZCB5 is also acknowledged. J. W. acknowledges the computing resources support from the National Supercomputer Center of Tianjin.

## REFERENCES

- Alden, Jonathan S., Adam W. Tsen, Pinshane Y. Huang, Robert Hovden, Lola Brown, Jiwoong Park, David A. Muller, and Paul L. McEuen, 2013, “Strain solitons and topological defects in bilayer graphene,” *Proc. Natl. Acad. Sci. U.S.A.* **110**, 11256–11260.
- Amontons, Guillaume, 1699, “De la resistance cause’e dans les machines [On the resistance caused in machines],” *Hist. Acad. R. Sci.* 206–227.
- Andrei, Eva Y., and Allan H. MacDonald, 2020, “Graphene bilayers with a twist,” *Nat. Mater.* **19**, 1265–1275.
- Angeli, M., D. Mandelli, A. Valli, A. Amaricci, M. Capone, E. Tosatti, and M. Fabrizio, 2018, “Emergent  $D_6$  symmetry in fully relaxed magic-angle twisted bilayer graphene,” *Phys. Rev. B* **98**, 235137.
- Aubry, Serge, 1983, “The twist map, the extended Frenkel-Kontorova model and the devil’s staircase,” *Physica (Amsterdam)* **7D**, 240–258.
- Baboukani, Sattari, Behnoosh, Zhijiang Ye, Kristofer G. Reyes, and Prathima C. Nalam, 2020, “Prediction of nanoscale friction for two-dimensional materials using a machine learning approach,” *Tribol. Lett.* **68**, 57.
- Baykara, Mehmet Z., Mohammad R. Vazirisereshk, and Ashlie Martini, 2018, “Emerging superlubricity: A review of the state of the art and perspectives on future research,” *Appl. Phys. Rev.* **5**, 041102.
- Belviso, Florian, Antonio Cammarata, Jamil Missaoui, and Tomas Polcar, 2020, “Effect of electric fields in low-dimensional materials: Nanofrictional response as a case study,” *Phys. Rev. B* **102**, 155433.
- Benassi, A., Ming Ma, M. Urbakh, and A. Vanossi, 2015, “The breakdown of superlubricity by driving-induced commensurate dislocations,” *Sci. Rep.* **5**, 16134.
- Benassi, A., A. Vanossi, G.E. Santoro, and E. Tosatti, 2010, “Parameter-free dissipation in simulated sliding friction,” *Phys. Rev. B* **82**, 081401.
- Berman, Diana, Sanket A. Deshmukh, Subramanian K.R.S. Sankaranarayanan, Ali Erdemir, and Anirudha V. Sumant, 2015, “Macroscale superlubricity enabled by graphene nanoscroll formation,” *Science* **348**, 1118–1122.
- Bohlehn, Thomas, Jules Mikhael, and Clemens Bechinger, 2012, “Observation of kinks and antikinks in colloidal monolayers driven across ordered surfaces,” *Nat. Mater.* **11**, 126–130.
- Bonelli, F., N. Manini, E. Cadelano, and L. Colombo, 2009, “Atomistic simulations of the sliding friction of graphene flakes,” *Eur. Phys. J. B* **70**, 449–459.
- Bowden, Frank Philip, and David Tabor, 2001, *The Friction and Lubrication of Solids*, Vol. 1 (Oxford University Press, New York).
- Braun, O.M., Michel Peyrard, D.V. Stryzheus, and Erio Tosatti, 2012, “Collective effects at frictional interfaces,” *Tribol. Lett.* **48**, 11–25.
- Brazda, T., A. Silva, N. Manini, A. Vanossi, R. Guerra, E. Tosatti, and C. Bechinger, 2018, “Experimental Observation of the Aubry Transition in Two-Dimensional Colloidal Monolayers,” *Phys. Rev. X* **8**, 011050.
- Brenner, Donald W., Olga A. Shenderova, Judith A. Harrison, Steven J. Stuart, Boris Ni, and Susan B. Sinnott, 2002, “A second-generation reactive empirical bond order (REBO) potential energy expression for hydrocarbons,” *J. Phys. Condens. Matter* **14**, 783–802.
- Brilliantov, Nikolay V., Alexey A. Tsukanov, Artem K. Grebenko, Albert G. Nasibulin, and Igor A. Ostanin, 2023, “Atomistic Mechanism of Friction-Force Independence on the Normal Load and Other Friction Laws for Dynamic Structural Superlubricity,” *Phys. Rev. Lett.* **131**, 266201.
- Butler, Sheneve Z., *et al.*, 2013, “Progress, challenges, and opportunities in two-dimensional materials beyond graphene,” *ACS Nano* **7**, 2898–2926.
- Butz, Benjamin, Christian Dolle, Florian Niekiel, Konstantin Weber, Daniel Waldmann, Heiko B. Weber, Bernd Meyer, and Erdmann Spiecker, 2014, “Dislocations in bilayer graphene,” *Nature (London)* **505**, 533–537.
- Buzio, Renato, Andrea Gerbi, Cristina Bernini, Luca Repetto, and Andrea Vanossi, 2021, “Graphite superlubricity enabled by triboinduced nanocontacts,” *Carbon* **184**, 875–890.
- Buzio, Renato, Andrea Gerbi, Cristina Bernini, Luca Repetto, and Andrea Vanossi, 2022, “Sliding friction and superlubricity of colloidal AFM probes coated by tribo-induced graphitic transfer layers,” *Langmuir* **38**, 12570–12580.
- Cao, Xin, Emanuele Panizon, Andrea Vanossi, Nicola Manini, and Clemens Bechinger, 2019, “Orientational and directional locking of colloidal clusters driven across periodic surfaces,” *Nat. Phys.* **15**, 776–780.

- Cao, Xin, Andrea Silva, Emanuele Panizon, Andrea Vanossi, Nicola Manini, Erio Tosatti, and Clemens Bechinger, 2022, “Moiré-Pattern Evolution Couples Rotational and Translational Friction at Crystalline Interfaces,” *Phys. Rev. X* **12**, 021059.
- Cao, Yuan, Valla Fatemi, Shiang Fang, Kenji Watanabe, Takashi Taniguchi, Efthimos Kaxiras, and Pablo Jarillo-Herrero, 2018, “Unconventional superconductivity in magic-angle graphene superlattices,” *Nature (London)* **556**, 43–50.
- Cao, Yuan, *et al.*, 2018, “Correlated insulator behaviour at half-filling in magic-angle graphene superlattices,” *Nature (London)* **556**, 80–84.
- Červenka, J., and C. F. J. Flipse, 2009, “Structural and electronic properties of grain boundaries in graphite: Planes of periodically distributed point defects,” *Phys. Rev. B* **79**, 195429.
- Chen, Zhe, Arash Khajeh, Ashlie Martini, and Seong H. Kim, 2019, “Chemical and physical origins of friction on surfaces with atomic steps,” *Sci. Adv.* **5**, eaaw0513.
- Cheng, Yao, and Ming Ma, 2020, “Understanding the effects of intercalated molecules on structural superlubric contacts,” *Phys. Rev. Mater.* **4**, 113606.
- Cihan, Ebru, Semran İpek, Engin Durgun, and Mehmet Z. Baykara, 2016, “Structural lubricity under ambient conditions,” *Nat. Commun.* **7**, 12055.
- Consoli, L., H. J. F. Knops, and A. Fasolino, 2000, “Onset of Sliding Friction in Incommensurate Systems,” *Phys. Rev. Lett.* **85**, 302–305.
- Deng, He, Ming Ma, Yiming Song, Qichang He, and Quanshui Zheng, 2018, “Structural superlubricity in graphite flakes assembled under ambient conditions,” *Nanoscale* **10**, 14314–14320.
- Derjaguin, B., 1934, “Molekulartheorie der äußeren reibung [Molecular theory of external friction],” *Z. Phys.* **88**, 661–675.
- de Wijn, A. S., 2012, “(In)commensurability, scaling, and multiplicity of friction in nanocrystals and application to gold nanocrystals on graphite,” *Phys. Rev. B* **86**, 085429.
- Dienwiebel, Martin, Gertjan S. Verhoeven, Namboodiri Pradeep, Joost W. M. Frenken, Jennifer A. Heimberg, and Henny W. Zandbergen, 2004, “Superlubricity of Graphite,” *Phys. Rev. Lett.* **92**, 126101.
- Dietzel, Dirk, Ján Brndiar, Ivan Štich, and André Schirmeisen, 2017, “Limitations of structural superlubricity: Chemical bonds versus contact size,” *ACS Nano* **11**, 7642–7647.
- Dietzel, Dirk, Michael Feldmann, Udo D. Schwarz, Harald Fuchs, and André Schirmeisen, 2013, “Scaling Laws of Structural Lubricity,” *Phys. Rev. Lett.* **111**, 235502.
- Dietzel, Dirk, Astrid S. de Wijn, Matthias Vorholzer, and Andre Schirmeisen, 2018, “Friction fluctuations of gold nanoparticles in the superlubric regime,” *Nanotechnology* **29**, 155702.
- Dong, Yalin, Ajay Vadakkepatt, and Ashlie Martini, 2011, “Analytical models for atomic friction,” *Tribol. Lett.* **44**, 367.
- Dowson, D., 1979, *History of Tribology* (Longman, London).
- Dudko, O. K., A. E. Filippov, J. Klafter, and M. Urbakh, 2002, “Dynamic force spectroscopy: A Fokker-Planck approach,” *Chem. Phys. Lett.* **352**, 499–504.
- Erdemir, Ali, and Jean-Michel Martin, 2007, *Superlubricity* (Elsevier, New York).
- Eriksson, Mikael, Filip Bergman, and Staffan Jacobson, 2002, “On the nature of tribological contact in automotive brakes,” *Wear* **36–26**, 252.
- Falk, Kerstin, Felix Sedlmeier, Laurent Joly, Roland R. Netz, and Lydéric Bocquet, 2010, “Molecular origin of fast water transport in carbon nanotube membranes: Superlubricity versus curvature dependent friction,” *Nano Lett.* **10**, 4067–4073.
- Feng, Shizhe, and Zhiping Xu, 2022, “Robustness of structural superlubricity beyond rigid models,” *Friction* **10**, 1382–1392.
- Filippov, Alexander E., Martin Dienwiebel, Joost W. M. Frenken, Joseph Klafter, and Michael Urbakh, 2008, “Torque and Twist against Superlubricity,” *Phys. Rev. Lett.* **100**, 046102.
- Filletter, T., J. L. McChesney, A. Bostwick, E. Rotenberg, K. V. Emtsev, Th. Seyller, K. Horn, and R. Bennewitz, 2009, “Friction and Dissipation in Epitaxial Graphene Films,” *Phys. Rev. Lett.* **102**, 086102.
- Finney, Nathan R., Matthew Yankowitz, Lithurshanaa Muraleetharan, K. Watanabe, T. Taniguchi, Cory R. Dean, and James Hone, 2019, “Tunable crystal symmetry in graphene–boron nitride heterostructures with coexisting moiré superlattices,” *Nat. Nanotechnol.* **14**, 1029–1034.
- Gajurel, Prakash, Mina Kim, Qiang Wang, Weitao Dai, Haitao Liu, and Cheng Cen, 2017, “Vacancy-controlled contact friction in graphene,” *Adv. Funct. Mater.* **27**, 1702832.
- Gao, Enlai, Bozhao Wu, Yelingyi Wang, Xiangzheng Jia, Wengen Ouyang, and Ze Liu, 2021, “Computational prediction of superlubric layered heterojunctions,” *ACS Appl. Mater. Interfaces* **13**, 33600–33608.
- Gao, Jianping, W. D. Luedtke, D. Gourdon, M. Ruths, J. N. Israelachvili, and Uzi Landman, 2004, “Frictional forces and Amontons’ law: From the molecular to the macroscopic scale,” *J. Phys. Chem. B* **108**, 3410–3425.
- Gao, Xiang, Wengen Ouyang, Oded Hod, and Michael Urbakh, 2021, “Mechanisms of frictional energy dissipation at graphene grain boundaries,” *Phys. Rev. B* **103**, 045418.
- Gao, Xiang, Wengen Ouyang, Michael Urbakh, and Oded Hod, 2021, “Superlubric polycrystalline graphene interfaces,” *Nat. Commun.* **12**, 5694.
- Gao, Xiang, Michael Urbakh, and Oded Hod, 2022, “Stick-Slip Dynamics of Moiré Superstructures in Polycrystalline 2D Material Interfaces,” *Phys. Rev. Lett.* **129**, 276101.
- Geim, A. K., and I. V. Grigorieva, 2013, “van der Waals heterostructures,” *Nature (London)* **499**, 419–425.
- Geim, A. K., and K. S. Novoselov, 2007, “The rise of graphene,” *Nat. Mater.* **6**, 183–191.
- Gigli, L., N. Manini, A. Benassi, E. Tosatti, A. Vanossi, and R. Guerra, 2017, “Graphene nanoribbons on gold: Understanding superlubricity and edge effects,” *2D Mater.* **4**, 045003.
- Gigli, L., N. Manini, E. Tosatti, R. Guerra, and A. Vanossi, 2018, “Lifted graphene nanoribbons on gold: From smooth sliding to multiple stick-slip regimes,” *Nanoscale* **10**, 2073–2080.
- Gnecco, E., R. Bennewitz, T. Gyalog, Ch. Loppacher, M. Bammerlin, E. Meyer, and H.-J. Güntherodt, 2000, “Velocity Dependence of Atomic Friction,” *Phys. Rev. Lett.* **84**, 1172–1175.
- Gongyang, Yujie, Wengen Ouyang, Cangyu Qu, Michael Urbakh, Baogang Quan, Ming Ma, and Quanshui Zheng, 2020, “Temperature and velocity dependent friction of a microscale graphite-DLC heterostructure,” *Friction* **8**, 462–470.
- Guerra, Roberto, Ugo Tartaglino, Andrea Vanossi, and Erio Tosatti, 2010, “Ballistic nanofriction,” *Nat. Mater.* **9**, 634–637.
- Guerra, Roberto, Merel van Wijk, Andrea Vanossi, Annalisa Fasolino, and Erio Tosatti, 2017, “Graphene on *h*-BN: To align or not to align?,” *Nanoscale* **9**, 8799–8804.
- Hashimoto, Ayako, Kazu Suenaga, Alexandre Gloter, Koki Urita, and Sumio Iijima, 2004, “Direct evidence for atomic defects in graphene layers,” *Nature (London)* **430**, 870–873.
- He, Gang, Martin H. Müser, and Mark O. Robbins, 1999, “Adsorbed layers and the origin of static friction,” *Science* **284**, 1650–1652.
- Hermann, Klaus, 2012, “Periodic overlayers and moiré patterns: Theoretical studies of geometric properties,” *J. Phys. Condens. Matter* **24**, 314210.

- Hirano, Motohisa, and Kazumasa Shinjo, 1990, "Atomistic locking and friction," *Phys. Rev. B* **41**, 11837–11851.
- Hirano, Motohisa, Kazumasa Shinjo, Reizo Kaneko, and Yoshitada Murata, 1997, "Observation of Superlubricity by Scanning Tunneling Microscopy," *Phys. Rev. Lett.* **78**, 1448–1451.
- Hod, Oded, 2013, "The registry index: A quantitative measure of materials' interfacial commensurability," *ChemPhysChem* **14**, 2376–2391.
- Hod, Oded, Ernst Meyer, Quanshui Zheng, and Michael Urbakh, 2018, "Structural superlubricity and ultralow friction across the length scales," *Nature (London)* **563**, 485–492.
- Huag, Xuanyu, Tengfei Li, Jin Wang, Kai Xia, Zipei Tan, Deli Peng, Xiaojian Xiang, Bin Liu, Ming Ma, and Quanshui Zheng, 2023, "Robust microscale structural superlubricity between graphite and nanostructured surface," *Nat. Commun.* **14**, 2931.
- Huang, Xuanyu, Li Lin, and Quanshui Zheng, 2020, "Theoretical study of superlubric nanogenerators with superb performances," *Nano Energy* **70**, 104494.
- Huang, Xuanyu, Xiaojian Xiang, Jinhui Nie, Deli Peng, Fuwei Yang, Zhanghui Wu, Haiyang Jiang, Zhiping Xu, and Quanshui Zheng, 2021, "Microscale schottky superlubric generator with high direct-current density and ultralong life," *Nat. Commun.* **12**, 2268.
- Hurtado, Juan A., and Kyung-Suk Kim, 1999, "Scale effects in friction of single-asperity contacts. I. From concurrent slip to single-dislocation-assisted slip," *Proc. R. Soc. A* **455**, 3363–3384.
- Jain, Sandeep K., Vladimir Juričić, and Gerard T. Barkema, 2016, "Structure of twisted and buckled bilayer graphene," *2D Mater.* **4**, 015018.
- Kawai, Shigeki, *et al.*, 2016, "Superlubricity of graphene nanoribbons on gold surfaces," *Science* **351**, 957–961.
- Kazmierczak, Nathanael P., Madeline Van Winkle, Colin Ophus, Karen C. Bustillo, Stephen Carr, Hamish G. Brown, Jim Ciston, Takashi Taniguchi, Kenji Watanabe, and D. Kwabena Bediako, 2021, "Strain fields in twisted bilayer graphene," *Nat. Mater.* **20**, 956–963.
- Kerelsky, Alexander, *et al.*, 2019, "Maximized electron interactions at the magic angle in twisted bilayer graphene," *Nature (London)* **572**, 95–100.
- Kietzig, Anne-Marie, Savvas G. Hatzikiriakos, and Peter Englezos, 2010, "Physics of ice friction," *J. Appl. Phys.* **107**, 081101.
- Kim, Kwanpyo, Sinisa Coh, Liang Z. Tan, William Regan, Jong Min Yuk, Eric Chatterjee, M. F. Crommie, Marvin L. Cohen, Steven G. Louie, and A. Zettl, 2012, "Raman Spectroscopy Study of Rotated Double-Layer Graphene: Misorientation-Angle Dependence of Electronic Structure," *Phys. Rev. Lett.* **108**, 246103.
- Koren, E., and U. Duerig, 2016a, "Moiré scaling of the sliding force in twisted bilayer graphene," *Phys. Rev. B* **94**, 045401.
- Koren, Elad, and Urs Duerig, 2016b, "Superlubricity in quasicrystalline twisted bilayer graphene," *Phys. Rev. B* **93**, 201404.
- Koren, Elad, Emanuel Lörtscher, Colin Rawlings, Armin W. Knoll, and Urs Duerig, 2015, "Adhesion and friction in mesoscopic graphite contacts," *Science* **348**, 679–683.
- Krim, Jacqueline, 2012, "Friction and energy dissipation mechanisms in adsorbed molecules and molecularly thin films," *Adv. Phys.* **61**, 155–323.
- Krylov, S. Yu., K. B. Jinesh, H. Valk, M. Dienwiebel, and J. W. M. Frenken, 2005, "Thermally induced suppression of friction at the atomic scale," *Phys. Rev. E* **71**, 065101.
- Krylov, Sergey Yu., and Joost W. M. Frenken, 2014, "The physics of atomic-scale friction: Basic considerations and open questions," *Phys. Status Solidi (b)* **251**, 711–736.
- Lang, Haojie, Yimeng Xu, Pengzhe Zhu, Yitian Peng, Kun Zou, Kang Yu, and Yao Huang, 2021, "Superior lubrication and electrical stability of graphene as highly effective solid lubricant at sliding electrical contact interface," *Carbon* **183**, 53–61.
- Larkin, A. I., and Yu. N. Ovchinnikov, 1979, "Pinning in type II superconductors," *J. Low Temp. Phys.* **34**, 409–428.
- Lee, Changgu, Qunyang Li, William Kalb, Xin-Zhou Liu, Helmuth Berger, Robert W. Carpick, and James Hone, 2010, "Frictional characteristics of atomically thin sheets," *Science* **328**, 76–80.
- Leven, Itai, Ido Azuri, Leeor Kronik, and Oded Hod, 2014, "Interlayer potential for hexagonal boron nitride," *J. Chem. Phys.* **140**, 104106.
- Leven, Itai, Dana Krepel, Ortal Shemesh, and Oded Hod, 2013, "Robust superlubricity in graphene/*h*-BN heterojunctions," *J. Phys. Chem. Lett.* **4**, 115–120.
- Leven, Itai, Tal Maaravi, Ido Azuri, Leeor Kronik, and Oded Hod, 2016, "Interlayer potential for graphene/*h*-BN heterostructures," *J. Chem. Theory Comput.* **12**, 2896–2905.
- Levita, Giacomo, Elisa Molinari, Tomas Polcar, and Maria Clelia Righi, 2015, "First-principles comparative study on the interlayer adhesion and shear strength of transition-metal dichalcogenides and graphene," *Phys. Rev. B* **92**, 085434.
- Li, Baowen, Jun Yin, Xiaofei Liu, Hongrong Wu, Jidong Li, Xuemei Li, and Wanlin Guo, 2019, "Probing van der Waals interactions at two-dimensional heterointerfaces," *Nat. Nanotechnol.* **14**, 567–572.
- Li, He, Jinhuan Wang, Song Gao, Qing Chen, Lianmao Peng, Kaihui Liu, and Xianlong Wei, 2017, "Superlubricity between MoS<sub>2</sub> monolayers," *Adv. Mater.* **29**, 1701474.
- Li, Jianfeng, Jinjin Li, Liang Jiang, and Jianbin Luo, 2020, "Fabrication of a graphene layer probe to measure force interactions in layered heterojunctions," *Nanoscale* **12**, 5435–5443.
- Li, Jinjin, Tianyang Gao, and Jianbin Luo, 2018, "Superlubricity of graphite induced by multiple transferred graphene nanoflakes," *Adv. Sci. Lett.* **5**, 1700616.
- Li, Jinjin, Jianfeng Li, Xinchun Chen, Yuhong Liu, and Jianbin Luo, 2020, "Microscale superlubricity at multiple gold-graphite heterointerfaces under ambient conditions," *Carbon* **161**, 827–833.
- Li, Qiang, Jie Song, Flemming Besenbacher, and Mingdong Dong, 2015, "Two-dimensional material confined water," *Acc. Chem. Res.* **48**, 119–127.
- Li, Zhiting, *et al.*, 2013, "Effect of airborne contaminants on the wettability of supported graphene and graphite," *Nat. Mater.* **12**, 925–931.
- Liao, Mengzhou, *et al.*, 2022, "Ultra-low friction and edge-pinning effect in large-lattice-mismatch van der Waals heterostructures," *Nat. Mater.* **21**, 47–53.
- Liu, Shu-Wei, *et al.*, 2017, "Robust microscale superlubricity under high contact pressure enabled by graphene-coated microsphere," *Nat. Commun.* **8**, 14029.
- Liu, Xiao, Thomas H. Metcalf, Jeremy T. Robinson, Brian H. Houston, and Fabrizio Scarpa, 2012, "Shear modulus of monolayer graphene prepared by chemical vapor deposition," *Nano Lett.* **12**, 1013–1017.
- Liu, Y., A. Erdemir, and E. I. Meletis, 1996, "A study of the wear mechanism of diamond-like carbon films," *Surf. Coat. Technol.* **82**, 48–56.
- Liu, Yanmin, Aisheng Song, Zhi Xu, Ruilong Zong, Jie Zhang, Wenyan Yang, Rong Wang, Yuanzhong Hu, Jianbin Luo, and Tianbao Ma, 2018, "Interlayer friction and superlubricity in single-crystalline contact enabled by two-dimensional flake-wrapped atomic force microscope tips," *ACS Nano* **12**, 7638–7646.
- Liu, Yanmin, Kang Wang, Qiang Xu, Jie Zhang, Yuanzhong Hu, Tianbao Ma, Quanshui Zheng, and Jianbin Luo, 2020, "Superlubricity between graphite layers in ultrahigh vacuum," *ACS Appl. Mater. Interfaces* **12**, 43167–43172.



- Liu, Yuan, Nathan O. Weiss, Xidong Duan, Hung-Chieh Cheng, Yu Huang, and Xiangfeng Duan, 2016, “van der Waals heterostructures and devices,” *Nat. Rev. Mater.* **1**, 16042.
- Liu, Ze, Peter Bøggild, Jia rui Yang, Yao Cheng, Francois Grey, Yilun Liu, Li Wang, and Quan shui Zheng, 2011, “A graphite nanoeraser,” *Nanotechnology* **22**, 265706.
- Liu, Ze, Jefferson Zhe Liu, Yao Cheng, Zhihong Li, Li Wang, and Quanshui Zheng, 2012, “Interlayer binding energy of graphite: A mesoscopic determination from deformation,” *Phys. Rev. B* **85**, 205418.
- Liu, Ze, Jiarui Yang, Francois Grey, Jefferson Zhe Liu, Yilun Liu, Yibing Wang, Yanlian Yang, Yao Cheng, and Quanshui Zheng, 2012, “Observation of Microscale Superlubricity in Graphite,” *Phys. Rev. Lett.* **108**, 205503.
- Losi, Gabriele, Paolo Restuccia, and M. C. Righi, 2020, “Superlubricity in phosphorene identified by means of *ab initio* calculations,” *2D Mater.* **7**, 025033.
- Luan, Binqun, and Mark O. Robbins, 2005, “The breakdown of continuum models for mechanical contacts,” *Nature (London)* **435**, 929–932.
- Luo, Zhengtang, Seungchul Kim, Nicole Kawamoto, Andrew M. Rappe, and A. T. Charlie Johnson, 2011, “Growth mechanism of hexagonal-shape graphene flakes with zigzag edges,” *ACS Nano* **5**, 9154–9160.
- Ma, Ming, Andrea Benassi, Andrea Vanossi, and Michael Urbakh, 2015, “Critical Length Limiting Superlow Friction,” *Phys. Rev. Lett.* **114**, 055501.
- Ma, Ming, Igor M. Sokolov, Wen Wang, Alexander E. Filippov, Quanshui Zheng, and Michael Urbakh, 2015, “Diffusion through Bifurcations in Oscillating Nano- and Microscale Contacts: Fundamentals and Applications,” *Phys. Rev. X* **5**, 031020.
- Maity, Indrajit, Mit H. Naik, Prabal K. Maiti, H. R. Krishnamurthy, and Manish Jain, 2020, “Phonons in twisted transition-metal dichalcogenide bilayers: Ultrasoft phasons and a transition from a superlubric to a pinned phase,” *Phys. Rev. Res.* **2**, 013335.
- Mandelli, D., I. Leven, O. Hod, and M. Urbakh, 2017, “Sliding friction of graphene/hexagonal–boron nitride heterojunctions: A route to robust superlubricity,” *Sci. Rep.* **7**, 10851.
- Mandelli, Davide, Roberto Guerra, Wengen Ouyang, Michael Urbakh, and Andrea Vanossi, 2018, “Static friction boost in edge-driven incommensurate contacts,” *Phys. Rev. Mater.* **2**, 046001.
- Mandelli, Davide, Wengen Ouyang, Oded Hod, and Michael Urbakh, 2019, “Negative Friction Coefficients in Superlubric Graphite–Hexagonal Boron Nitride Heterojunctions,” *Phys. Rev. Lett.* **122**, 076102.
- Mandelli, Davide, Andrea Vanossi, Nicola Manini, and Erio Tosatti, 2015, “Friction Boosted by Equilibrium Misalignment of Incommensurate Two-Dimensional Colloid Monolayers,” *Phys. Rev. Lett.* **114**, 108302.
- Mao, Wendy L., Ho kwang Mao, Peter J. Eng, Thomas P. Trainor, Matthew Newville, Chi chang Kao, Dion L. Heinz, Jinfu Shu, Yue Meng, and Russell J. Hemley, 2003, “Bonding changes in compressed superhard graphite,” *Science* **302**, 425–427.
- Martin, J. M., C. Donnet, Th. Le Mogne, and Th. Epicier, 1993, “Superlubricity of molybdenum disulphide,” *Phys. Rev. B* **48**, 10583–10586.
- Martin, Jean Michel, and Ali Erdemir, 2018, “Superlubricity: Friction’s vanishing act,” *Phys. Today* **71**, No. 4, 40–46.
- Martins, Luiz Gustavo Pimenta, *et al.*, 2017, “Raman evidence for pressure-induced formation of diamondene,” *Nat. Commun.* **8**, 96.
- McMillan, W. L., 1976, “Theory of discommensurations and the commensurate-incommensurate charge-density-wave phase transition,” *Phys. Rev. B* **14**, 1496–1502.
- Memarian, F., A. Fereidoon, and M. Darvish Ganji, 2015, “Graphene Young’s modulus: Molecular mechanics and DFT treatments,” *Superlattices Microstruct.* **85**, 348–356.
- Mogera, Umesha, and Giridhar U. Kulkarni, 2020, “A new twist in graphene research: Twisted graphene,” *Carbon* **156**, 470–487.
- Müser, M. H., 2004, “Structural lubricity: Role of dimension and symmetry,” *Europhys. Lett.* **66**, 97–103.
- Müser, Martin H., 2011, “Velocity dependence of kinetic friction in the Prandtl-Tomlinson model,” *Phys. Rev. B* **84**, 125419.
- Müser, Martin H., Ludgar Wenning, and Mark O. Robbins, 2001, “Simple Microscopic Theory of Amontons’s Laws for Static Friction,” *Phys. Rev. Lett.* **86**, 1295–1298.
- Niguès, A., A. Siria, P. Vincent, P. Poncharal, and L. Bocquet, 2014, “Ultrahigh interlayer friction in multiwalled boron nitride nanotubes,” *Nat. Mater.* **13**, 688–693.
- Nimbalkar, Amol, and Hyunmin Kim, 2020, “Opportunities and challenges in twisted bilayer graphene: A review,” *Nano-Micro Lett.* **12**, 126.
- Novoselov, K. S., A. Mishchenko, A. Carvalho, and A. H. Castro Neto, 2016, “2D materials and van der Waals heterostructures,” *Science* **353**, aac9439.
- Ouyang, Wengen, Ido Azuri, Davide Mandelli, Alexandre Tkatchenko, Leeor Kronik, Michael Urbakh, and Oded Hod, 2020, “Mechanical and tribological properties of layered materials under high pressure: Assessing the importance of many-body dispersion effects,” *J. Chem. Theory Comput.* **16**, 666–676.
- Ouyang, Wengen, Oded Hod, and Roberto Guerra, 2021, “Registry-dependent potential for interfaces of gold with graphitic systems,” *J. Chem. Theory Comput.* **17**, 7215–7223.
- Ouyang, Wengen, Davide Mandelli, Michael Urbakh, and Oded Hod, 2018, “Nanoserpents: Graphene nanoribbon motion on two-dimensional hexagonal materials,” *Nano Lett.* **18**, 6009–6016.
- Ouyang, Wengen, Astrid S. de Wijn, and Michael Urbakh, 2018, “Atomic-scale sliding friction on a contaminated surface,” *Nanoscale* **10**, 6375–6381.
- Özoğul, Alper, Semran İpek, Engin Durgun, and Mehmet Z. Baykara, 2017, “Structural superlubricity of platinum on graphite under ambient conditions: The effects of chemistry and geometry,” *Appl. Phys. Lett.* **111**, 211602.
- Park, Jeong Min, Yuan Cao, Kenji Watanabe, Takashi Taniguchi, and Pablo Jarillo-Herrero, 2021, “Tunable strongly coupled superconductivity in magic-angle twisted trilayer graphene,” *Nature (London)* **590**, 249–255.
- Pellegrini, Franco, Emanuele Panizon, Giuseppe E. Santoro, and Erio Tosatti, 2019, “Thermally assisted lubricity and negative work tails in sliding friction,” *Phys. Rev. B* **99**, 075428.
- Peng, Deli, Jin Wang, Haiyang Jiang, Shuji Zhao, Zhanghui Wu, Kaiwen Tian, Ming Ma, and Quanshui Zheng, 2022, “100 km wear-free sliding achieved by microscale superlubric graphite/DLC heterojunctions under ambient conditions,” *Nat. Sci. Rev.* **9**, nwab109.
- Peng, Deli, Zhanghui Wu, Diwei Shi, Cangyu Qu, Haiyang Jiang, Yiming Song, Ming Ma, Gabriel Aeppli, Michael Urbakh, and Quanshui Zheng, 2020, “Load-induced dynamical transitions at graphene interfaces,” *Proc. Natl. Acad. Sci. U.S.A.* **117**, 12618–12623.
- Persson, B. N. J., and E. Tosatti, 1999, “Theory of friction: Elastic coherence length and earthquake dynamics,” *Solid State Commun.* **109**, 739–744.

- Peyrard, M., and S. Aubry, 1983, “Critical behaviour at the transition by breaking of analyticity in the discrete Frenkel-Kontorova model,” *J. Phys. C* **16**, 1593–1608.
- Pham, Phuong V., Srikrishna Chanakya Bodepudi, Khurram Shehzad, Yuan Liu, Yang Xu, Bin Yu, and Xiangfeng Duan, 2022, “2d heterostructures for ubiquitous electronics and optoelectronics: Principles, opportunities, and challenges,” *Chem. Rev.* **122**, 6514–6613.
- Pierno, Matteo, Lorenzo Bruschi, Giampaolo Mistura, Guido Paolicelli, Alessandro di Bona, Sergio Valeri, Roberto Guerra, Andrea Vanossi, and Erio Tosatti, 2015, “Frictional transition from superlubric islands to pinned monolayers,” *Nat. Nanotechnol.* **10**, 714–718.
- Plimpton, Steve, 1995, “Fast parallel algorithms for short-range molecular dynamics,” *J. Comput. Phys.* **117**, 1–19.
- Popov, Andrey M., Irina V. Lebedeva, Andrey A. Knizhnik, Yurii E. Lozovik, and Boris V. Potapkin, 2012, “Barriers to motion and rotation of graphene layers based on measurements of shear mode frequencies,” *Chem. Phys. Lett.* **536**, 82–86.
- Prandtl, L., 1928, “Ein gedankenmodell zur kinetischen theorie der festen körper [Hypothetical model for the kinetic theory of solid bodies],” *Z. Angew. Math. Mech.* **8**, 85–106.
- Qu, Cangyu, Kunqi Wang, Jin Wang, Yujie Gongyang, Robert W. Carpick, Michael Urbakh, and Quanshui Zheng, 2020, “Origin of Friction in Superlubric Graphite Contacts,” *Phys. Rev. Lett.* **125**, 126102.
- Rao, C. N. R., A. K. Sood, K. S. Subrahmanyam, and A. Govindaraj, 2009, “Graphene: The new two-dimensional nanomaterial,” *Angew. Chem., Int. Ed.* **48**, 7752–7777.
- Reguzzoni, M., A. Fasolino, E. Molinari, and M. C. Righi, 2012, “Potential energy surface for graphene on graphene: *Ab initio* derivation, analytical description, and microscopic interpretation,” *Phys. Rev. B* **86**, 245434.
- Reimann, Peter, and Mykhaylo Evstigneev, 2004, “Nonmonotonic Velocity Dependence of Atomic Friction,” *Phys. Rev. Lett.* **93**, 230802.
- Ribeiro-Palau, Rebeca, Changjian Zhang, Kenji Watanabe, Takashi Taniguchi, James Hone, and Cory R. Dean, 2018, “Twistable electronics with dynamically rotatable heterostructures,” *Science* **361**, 690–693.
- Riedl, C., C. Coletti, T. Iwasaki, A. A. Zakharov, and U. Starke, 2009, “Quasi-Free-Standing Epitaxial Graphene on SiC Obtained by Hydrogen Intercalation,” *Phys. Rev. Lett.* **103**, 246804.
- Riedo, E., E. Gneco, R. Bennewitz, E. Meyer, and H. Brune, 2003, “Interaction Potential and Hopping Dynamics Governing Sliding Friction,” *Phys. Rev. Lett.* **91**, 084502.
- Righi, M. Clelia, 2021, “*Ab initio* insights into graphene lubricity,” in *Superlubricity*, 2nd ed., edited by Ali Erdemir, Jean Michel Martin, and Jianbin Luo (Elsevier, New York), Chap. 2, pp. 21–38.
- Rowe, Patrick, Gábor Csányi, Dario Alfè, and Angelos Michaelides, 2018, “Development of a machine learning potential for graphene,” *Phys. Rev. B* **97**, 054303.
- Sang, Yi, Martin Dubé, and Martin Grant, 2001, “Thermal Effects on Atomic Friction,” *Phys. Rev. Lett.* **87**, 174301.
- Sharp, Tristan A., Lars Pastewka, and Mark O. Robbins, 2016, “Elasticity limits structural superlubricity in large contacts,” *Phys. Rev. B* **93**, 121402.
- Shinjo, Kazumasa, and Motohisa Hirano, 1993, “Dynamics of friction: Superlubric state,” *Surf. Sci.* **283**, 473–478.
- Sokoloff, J. B., 1990, “Theory of energy dissipation in sliding crystal surfaces,” *Phys. Rev. B* **42**, 760–765.
- Sokoloff, J. B., J. E. Sacco, and J. F. Weisz, 1978, “Undamped Lattice Vibrations in Systems with Two Incommensurate Periodicities,” *Phys. Rev. Lett.* **41**, 1561–1564.
- Song, Aisheng, Ruoyu Shi, Hongliang Lu, Xueyan Wang, Yuanzhong Hu, Hong-Jun Gao, Jianbin Luo, and Tianbao Ma, 2022, “Fluctuation of interfacial electronic properties induces friction tuning under an electric field,” *Nano Lett.* **22**, 1889–1896.
- Song, Yiming, Davide Mandelli, Oded Hod, Michael Urbakh, Ming Ma, and Quanshui Zheng, 2018, “Robust microscale superlubricity in graphite/hexagonal boron nitride layered heterojunctions,” *Nat. Mater.* **17**, 894–899.
- Song, Yiming, Jin Wang, Yiran Wang, Michael Urbakh, Quanshui Zheng, and Ming Ma, 2021, “Directional anisotropy of friction in microscale superlubric graphite/*h*-BN heterojunctions,” *Phys. Rev. Mater.* **5**, 084002.
- Stampfli, Peter, 1986, “A dodecagonal quasiperiodic lattice in two dimensions,” *Helv. Phys. Acta* **59**, 1260–1263.
- Stepanov, Petr, Ipsita Das, Xiaobo Lu, Ali Fahimniya, Kenji Watanabe, Takashi Taniguchi, Frank H. L. Koppens, Johannes Lischner, Leonid Levitov, and Dmitri K. Efetov, 2020, “Untying the insulating and superconducting orders in magic-angle graphene,” *Nature (London)* **583**, 375–378.
- Stuart, Steven J., Alan B. Tutein, and Judith A. Harrison, 2000, “A reactive potential for hydrocarbons with intermolecular interactions,” *J. Chem. Phys.* **112**, 6472–6486.
- Sun, Junhui, Yanning Zhang, Zhibin Lu, Qunyang Li, Qunji Xue, Shiyu Du, Jibin Pu, and Liping Wang, 2018, “Superlubricity enabled by pressure-induced friction collapse,” *J. Phys. Chem. Lett.* **9**, 2554–2559.
- Tan, P. H., *et al.*, 2012, “The shear mode of multilayer graphene,” *Nat. Mater.* **11**, 294–300.
- Theodorou, G., and T. M. Rice, 1978, “Statics and dynamics of incommensurate lattices,” *Phys. Rev. B* **18**, 2840–2856.
- Thompson, Aidan P., *et al.*, 2022, “LAMMPS—A flexible simulation tool for particle-based materials modeling at the atomic, meso, and continuum scales,” *Comput. Phys. Commun.* **271**, 108171.
- Tison, Yann, Jérôme Lagoute, Vincent Repain, Cyril Chacon, Yann Girard, Frédéric Joucken, Robert Sporcken, Fernando Gargiulo, Oleg V. Yazyev, and Sylvie Rousset, 2014, “Grain boundaries in graphene on SiC(000 $\bar{1}$ ) substrate,” *Nano Lett.* **14**, 6382–6386.
- Tomlinson, G. A., 1929, “CVI. A molecular theory of friction,” *London Edinburgh Philos. Mag. J. Sci.* **7**, 905–939.
- Törmä, Päivi, Sebastiano Peotta, and Bogdan A. Bernevig, 2022, “Superconductivity, superfluidity and quantum geometry in twisted multilayer systems,” *Nat. Rev. Phys.* **4**, 528–542.
- Trambly de Laissardière, G., D. Mayou, and L. Magaud, 2010, “Localization of Dirac electrons in rotated graphene bilayers,” *Nano Lett.* **10**, 804–808.
- Uchida, Kazuyuki, Shinnosuke Furuya, Jun-Ichi Iwata, and Atsushi Oshiyama, 2014, “Atomic corrugation and electron localization due to moiré patterns in twisted bilayer graphenes,” *Phys. Rev. B* **90**, 155451.
- Urbakh, Michael, 2013, “Towards macroscale superlubricity,” *Nat. Nanotechnol.* **8**, 893–894.
- van den Ende, Joost A., Astrid S. de Wijn, and Annalisa Fasolino, 2012, “The effect of temperature and velocity on superlubricity,” *J. Phys. Condens. Matter* **24**, 445009.
- Vanossi, Andrea, Clemens Bechinger, and Michael Urbakh, 2020, “Structural lubricity in soft and hard matter systems,” *Nat. Commun.* **11**, 4657.
- Vanossi, Andrea, Nicola Manini, Michael Urbakh, Stefano Zapperi, and Erio Tosatti, 2013, “Colloquium: Modeling friction: From nanoscale to mesoscale,” *Rev. Mod. Phys.* **85**, 529–552.

- Vanossi, Andrea, and Erio Tosatti, 2012, “Kinks in motion,” *Nat. Mater.* **11**, 97–98.
- van Wijk, M. M., M. Dienwiebel, J. W. M. Frenken, and A. Fasolino, 2013, “Superlubric to stick-slip sliding of incommensurate graphene flakes on graphite,” *Phys. Rev. B* **88**, 235423.
- Varini, Nicola, Andrea Vanossi, Roberto Guerra, Davide Mandelli, Rosario Capozza, and Erio Tosatti, 2015, “Static friction scaling of physisorbed islands: The key is in the edge,” *Nanoscale* **7**, 2093–2101.
- Vu, Cuong Cao, Shoumo Zhang, Michael Urbakh, Qunyang Li, Q.-C. He, and Quanshui Zheng, 2016, “Observation of normal-force-independent superlubricity in mesoscopic graphite contacts,” *Phys. Rev. B* **94**, 081405.
- Wang, Duoming, *et al.*, 2016, “Thermally Induced Graphene Rotation on Hexagonal Boron Nitride,” *Phys. Rev. Lett.* **116**, 126101.
- Wang, Jianjun, Jinming Li, Chong Li, Xiaolin Cai, Wenguang Zhu, and Yu Jia, 2016, “Tuning the nanofriction between two graphene layers by external electric fields: A density functional theory study,” *Tribol. Lett.* **61**, 4.
- Wang, Jin, Wei Cao, Yiming Song, Cangyu Qu, Quanshui Zheng, and Ming Ma, 2019, “Generalized scaling law of structural superlubricity,” *Nano Lett.* **19**, 7735–7741.
- Wang, Jin, Ali Khosravi, Andrea Silva, Michele Fabrizio, Andrea Vanossi, and Erio Tosatti, 2023, “Bending stiffness collapse, buckling, topological bands of freestanding twisted bilayer graphene,” *Phys. Rev. B* **108**, L081407.
- Wang, Jin, Andrea Vanossi, and Erio Tosatti, 2024, “Effective stick-slip parameter for structurally lubric 2D interface friction,” *arXiv*: 2401.13780.
- Wang, Jin, Ming Ma, and Erio Tosatti, 2023, “Kinetic friction of structurally superlubric 2D material interfaces,” *J. Mech. Phys. Solids* **180**, 105396.
- Wang, Jingang, Fengcai Ma, and Mengtao Sun, 2017, “Graphene, hexagonal boron nitride, and their heterostructures: Properties and applications,” *RSC Adv.* **7**, 16801–16822.
- Wang, Kehan, Jin Wang, and Ming Ma, 2022, “Negative or positive? Loading area dependent correlation between friction and normal load in structural superlubricity,” *Front. Chem.* **9**, 807630.
- Wang, Kunqi, Yuqing He, Wei Cao, Jin Wang, Cangyu Qu, Maosheng Chai, Yuan Liu, Quanshui Zheng, and Ming Ma, 2022, “Structural superlubricity with a contaminant-rich interface,” *J. Mech. Phys. Solids* **169**, 105063.
- Wang, Kunqi, Cangyu Qu, Jin Wang, Wengen Ouyang, Ming Ma, and Quanshui Zheng, 2019, “Strain engineering modulates graphene interlayer friction by moiré pattern evolution,” *ACS Appl. Mater. Interfaces* **11**, 36169–36176.
- Wang, Kunqi, Cangyu Qu, Jin Wang, Baogang Quan, and Quanshui Zheng, 2020, “Characterization of a Microscale Superlubric Graphite Interface,” *Phys. Rev. Lett.* **125**, 026101.
- Wang, Wen, Shuyang Dai, Xide Li, Jiarui Yang, David J. Srolovitz, and Quanshui Zheng, 2015, “Measurement of the cleavage energy of graphite,” *Nat. Commun.* **6**, 7853.
- Wang, Wen, and Xide Li, 2019, “Interlayer motion and ultra-low sliding friction in microscale graphite flakes,” *Europhys. Lett.* **125**, 26003.
- Wen, Mingjian, Stephen Carr, Shiang Fang, Efthimios Kaxiras, and Ellad B. Tadmor, 2018, “Dihedral-angle-corrected registry-dependent interlayer potential for multilayer graphene structures,” *Phys. Rev. B* **98**, 235404.
- Weston, Astrid, *et al.*, 2020, “Atomic reconstruction in twisted bilayers of transition metal dichalcogenides,” *Nat. Nanotechnol.* **15**, 592–597.
- Woods, C. R., *et al.*, 2014, “Commensurate-incommensurate transition in graphene on hexagonal boron nitride,” *Nat. Phys.* **10**, 451–456.
- Wu, Zhanghui, Xuanyu Huang, Xiaojian Xiang, and Quanshui Zheng, 2021, “Electro-superlubric springs for continuously tunable resonators and oscillators,” *Commun. Mater.* **2**, 104.
- Xu, Peipei, Kang Yu, Xiushuo Zhang, Haojie Lang, Hong Li, and Yitian Peng, 2022, “A first-principles study on the superlubricity of two-dimensional graphene/ZrS<sub>2</sub> heterostructure,” *Tribol. Int.* **174**, 107727.
- Xu, Zhiping, Taotao Sun, Enlai Gao, Xiangzheng Jia, Zhou Wang, Ming Ma, and Quanshui Zheng, 2022, “Robust structural superlubricity under gigapascal pressures,” [10.21203/rs.3.rs-1683893/v1](https://doi.org/10.21203/rs.3.rs-1683893/v1).
- Yan, Weidong, Xiang Gao, Wengen Ouyang, Ze Liu, Oded Hod, and Michael Urbakh, 2024, “Shape-dependent friction scaling laws in twisted layered material interfaces,” *J. Mech. Phys. Solids* (in press).
- Yang, Xing, and Bin Zhang, 2021, “Rotational friction correlated with moiré patterns in strained bilayer graphene: Implications for nanoscale lubrication,” *ACS Appl. Nano Mater.* **4**, 8880–8887.
- Yankowitz, Matthew, Shaowen Chen, Hryhoriy Polshyn, Yuxuan Zhang, K. Watanabe, T. Taniguchi, David Graf, Andrea F. Young, and Cory R. Dean, 2019, “Tuning superconductivity in twisted bilayer graphene,” *Science* **363**, 1059–1064.
- Yankowitz, Matthew, Qiong Ma, Pablo Jarillo-Herrero, and Brian J. LeRoy, 2019, “van der Waals heterostructures combining graphene and hexagonal boron nitride,” *Nat. Rev. Phys.* **1**, 112–125.
- Yazyev, Oleg V., and Yong P. Chen, 2014, “Polycrystalline graphene and other two-dimensional materials,” *Nat. Nanotechnol.* **9**, 755–767.
- Yazyev, Oleg V., and Steven G. Louie, 2010, “Topological defects in graphene: Dislocations and grain boundaries,” *Phys. Rev. B* **81**, 195420.
- Yoo, Hyobin, *et al.*, 2019, “Atomic and electronic reconstruction at the van der waals interface in twisted bilayer graphene,” *Nat. Mater.* **18**, 448–453.
- Zhang, Kuan, and Ellad B. Tadmor, 2018, “Structural and electron diffraction scaling of twisted graphene bilayers,” *J. Mech. Phys. Solids* **112**, 225–238.
- Zhang, Rufan, Zhiyuan Ning, Yingying Zhang, Quanshui Zheng, Qing Chen, Huanhuan Xie, Qiang Zhang, Weizhong Qian, and Fei Wei, 2013, “Superlubricity in centimetres-long double-walled carbon nanotubes under ambient conditions,” *Nat. Nanotechnol.* **8**, 912–916.
- Zhang, Shuai, Tianbao Ma, Ali Erdemir, and Qunyang Li, 2019, “Tribology of two-dimensional materials: From mechanisms to modulating strategies,” *Mater. Today* **26**, 67–86.
- Zhang, Shuai, *et al.*, 2022, “Domino-like stacking order switching in twisted monolayer-multilayer graphene,” *Nat. Mater.* **21**, 621–626.
- Zhao, Yu, Hui Mei, Peng Chang, Chao Chen, Laifei Cheng, and Konstantinos G. Dassios, 2021, “Infinite approaching superlubricity by three-dimensional printed structures,” *ACS Nano* **15**, 240–257.
- Zheng, Quanshui, and Qing Jiang, 2002, “Multiwalled Carbon Nanotubes as Gigahertz Oscillators,” *Phys. Rev. Lett.* **88**, 045503.